Title: Cytoskeletal tension forces mitohormesis

Authors: Kevin M. Tharp[1], Ryo Higuchi-Sanabria[2], Greg Timblin[3], Carlos Garzon-Coral[4], Breanna Ford[5-6], Catherine Schneider[5], Jonathon M. Muncie[1], Connor Stashko[1], Joseph R. Daniele[7], Phillip A. Frankino[2], Sagar S. Manoli[8], Hao Shao[9], Jason Gestwicki[9], Marc Hellerstein[5], Daniel K. Nomura[5-6], Alexander R. Dunn[4], Karou Saijo[3], Andrew Dillin[2], and Valerie M. Weaver[1,10]*

Affiliations:

[1]Center for Bioengineering and Tissue Regeneration, Department of Surgery, University of California San Francisco, San Francisco, CA 94143, USA.

[2]Department of Molecular & Cellular Biology, Howard Hughes Medical Institute, University of California, Berkeley, Berkeley, CA 94597, USA.

[3]Department of Molecular and Cell Biology, University of California, Berkeley, Berkeley, CA 94720 USA

[4]Chemical Engineering Department, Stanford University, Stanford, CA 94305, USA.

[5]Department of Nutritional Sciences and Toxicology, University of California, Berkeley, Berkeley, CA 94720, USA.

[6]Novartis-Berkeley Center for Proteomics and Chemistry Technologies and Department of Chemistry, University of California, Berkeley, Berkeley, CA 94720, USA.

[7]MD Anderson Cancer Center, South Campus Research, Houston, CA 77054

[8]Department of Cell and Tissue Biology, University of California, San Francisco, San Francisco, CA 94143

[9]Department of Pharmaceutical Chemistry, University of California San Francisco, San Francisco, CA 94158, USA.

[10]Department of Bioengineering and Therapeutic Sciences and Department of Radiation Oncology, Eli and Edythe Broad Center of Regeneration Medicine and Stem Cell Research, and The Helen Diller Family Comprehensive Cancer Center, University of California San Francisco, San Francisco, CA 94143, USA.

*Correspondence to:

Valerie M. Weaver, University of California, San Francisco
513 Parnassus Avenue, 565 Health Sciences East
San Francisco, CA 94143-0456
Email: Valerie.Weaver@ucsf.edu
Telephone: 415 476-3826 Fax: 415-476-3985

bioRxiv "Preprint" Manuscript

Abstract: Mitochondria control eukaryotic cell fate by producing the energy needed to support life and the signals required to execute programmed cell death. The biochemical milieu regulates mitochondrial function and contributes to the dysfunctional mitochondrial phenotypes implicated in cancer and the morbidities of ageing. Extracellular matrix stiffness and cytoskeletal tension are also altered in cancer and in aged tissues. We determined that cytoskeletal tension elicits a mitochondrial stress response that modifies mitochondrial function *via* SLC9A1-dependent ion exchange and HSF1-dependent transcription. Our data indicate that this cytoskeletal tension-induced mitochondrial stress response, termed mitohormesis, adaptively tunes mitochondrial metabolism and facilitates oxidative stress resilience. These findings demonstrate that cytoskeletal tension regulates mitochondrial function and suggests that mechanical forces influence tissue behavior by modulating mitochondrial metabolism.

One Sentence Summary: Adhesion-mediated mechanotransduction programs mitochondrial metabolism through an adaptive stress response.

Main Text: Nutrient availability, oxygen content, and pH regulate cellular metabolism. Extracellular matrix (ECM) stiffness can change cellular metabolism by regulating the levels and/or activity of cytoplasmic enzymes responsive to cytoskeletal polymerization (*1*, *2*). Many aspects of cellular metabolism depend upon the mitochondria, a key metabolic organelle that is structurally altered by physical forces and the cytoskeleton (*3–5*). Since mitochondrial structure influences mitochondrial function, we sought to determine if ECM stiffness and cytoskeletal tension influence cellular metabolism by regulating mitochondrial structure and function.

Cytoskeletal tension alters mitochondrial structure and function

To explore associations between ECM stiffness and mitochondrial structure, we examined the mitochondrial morphology of nonmalignant human mammary epithelial cells (MECs; MCF10A) cultured for 24 hours on polyacrylamide hydrogel gels (PA-gel) ranging in elasticity (stiffness) between normal breast stroma (400 Pa) and breast tumors (6k – 60k Pa) (*6*, *7*) (tissue culture polystyrene ~3G Pa). MECs cultured on this range of PA-gel elasticities displayed a variety of mitochondrial morphologies, ranging from thin interconnected filaments (400 Pa), to thickened filaments (6k Pa), and then ~300 nM diameter fragments with toroidal shapes (60k Pa) (Fig.1A and S1A-B). Cells respond to ECM stiffness by ligating ECM adhesion receptors that induce Rho-GTPase-dependent cytoskeletal remodeling and increase actomyosin tension through type-II myosins (*8*). Pharmacological inhibition of Rho-associated protein kinase (ROCK) with Y27632 or type-II myosins with blebbistatin, reduced the prevalence of the thick toroidal mitochondrial fragments in MECs plated on the stiffest ECM PA-gels (Fig.1A). These data indicate that mitochondrial structure is sensitive to cytoskeletal tension generated in response to stiffness of the extracellular matrix.

We investigated the relationship between adhesion-dependent cytoskeletal tension and mitochondrial fragmentation by exogenously expressing a β1-integrin "gain of function" model. Expression of the β1-integrin (V737N, point mutation) promotes focal adhesion assembly, Rho-GTPase-dependent cytoskeletal remodeling, actomyosin tension (*9*), and a fragmented and toroidal mitochondrial morphology on soft PA-gels (Fig. 1B). By comparison, MECs expressing a wild-type β1 integrin did not form toroidal

mitochondrial structures in MECs on soft PA-gels. Mitochondrial function, which can be assayed by measuring mitochondrial oxygen consumption rates (respiration), indicated that β1(V737N)-integrin expressing MECs had lower respiratory rates than β1-integrin expressing MECs (Fig. 1C). Contrary to the paradigm that mitochondrial dysfunction (e.g. reduced respiration) and fragmentation/toroids occur in response to the loss of mitochondrial membrane potential (ΔΨm), the β1(V737N)-integrin expressing MECs had higher, not lower, mitochondrial membrane potential (Fig. 1D).

To test the relationship between integrin adhesion and mitochondrial function we varied the surface density of fibronectin (*10*), an ECM component and integrin ligand that is known modulate focal adhesion assembly and cytoskeletal tension. MECs plated on the highest density of fibronectin (60 µM/cm^2), in which focal adhesion assembly and actomyosin activity were high, showed a significant repression of mitochondrial respiration (Fig. S1C). Enhancing integrin activity and inducing focal adhesion assembly and cytoskeletal tension by treating MECs cultured on low density fibronectin (6 µM/cm^2) with manganese (*11*), suppressed mitochondrial respiration (Fig. S1D), as did increasing cytoskeletal reorganization and cytoskeletal tension by expressing an inducible ROCK, ROCK:ER (*12*) (Fig. S1E-H). These findings indicate that adhesion-dependent cytoskeletal tension modulates mitochondrial structure and function.

Hyperglycemia and stiff substrates facilitate similar mitochondrial morphologies

Hyperglycemia (25 mM glucose) is an extracellular biochemical stress that induces mitochondrial fragmentation and raises mitochondrial membrane potential in cultured cells (*13*). To explore whether the fragmented/toroidal mitochondrial morphologies induced by high cytoskeletal tension, were similar to those induced by hyperglycemia, we increased glucose concentration from 5 mM to 25 mM in MECs plated on the soft (400 Pa) PA-gels and examined changes in mitochondrial organization. Lattice light sheet microscopy (LLSM), which permits live cell imaging with limited phototoxicity (*14*), revealed that exposing MECs plated on soft (400 Pa) PA-gels to hyperglycemia induced a rapid transition of mitochondrial morphology from a filamentous network into fragmented toroidal structures (Fig. 1E), comparable to MECs on stiff PA-gels in 5 mM glucose media (Fig. 1A & S1A). Cells exposed to hyperglycemia or plated on stiff PA-gels express similar gene profiles that have been implicated in the mitochondrial unfolded protein response (UPR^{mt}) and oxidative stress resilience (OxSR) (*15*) (Fig.1F & S1I-J). Since both hyperglycemia and stiff PA-gels induce protective OxSR genes, we hypothesized that the reorganization of the mitochondria may also reflect a pro-survival response (*16*).

Given the evidence that ECM stiffness promoted mitochondrial reorganization by inducing cytoskeletal tension, we asked if hyperglycemia also affected cytoskeletal tension. Atomic force microscopy (AFM) indentation revealed that hyperglycemia significantly enhanced cortical tension in MECs (Fig. 1G). These findings were confirmed in a second cell line, the MDA-MB-231 MECs, which is a model of triple negative human breast cancer (Fig. S1K). Similar to the reduced respiration rate induced by manipulating cytoskeletal tension, hyperglycemia also reduced mitochondrial respiration rate (Fig. 1H). These findings demonstrate that biochemical and mechanical signals stimulate similar changes in mitochondrial structure and function, which may occur through the same adaptive stress response.

Cytoskeletal tension alters mitochondrial structure and function *via* SLC9A1

Mitochondrial fragmentation is thought to coordinate with mitophagy (autophagosome-mediated degradation of mitochondria) to repair dysfunctional mitochondria that have reduced mitochondrial membrane potential or increased reactive oxygen species (ROS) production/leak (*17–19*). However, our data indicated that the mitochondrial fragmentation induced by increased cytoskeletal tension had elevated mitochondrial membrane potential (Fig 2A). Thus, we reasoned that large mitochondrial fragments with toroidal morphologies likely arise through a different mechanism than has been previously described. Mitochondrial membrane potential reflects a pH differential between the mitochondrial inner membrane space and the mitochondrial matrix, and is therefore sensitive to changes in intracellular pH (pH_i). Both hyperglycemia and ROCK activity, increase cytoskeletal tension, as well as pH_i (*20, 21*). Therefore, we sought to test if the toroidal mitochondrial morphology and the elevated mitochondrial membrane potential could be due to cytoskeletal tension-dependent regulation of cellular pH_i.

We measured an increase in pH_i in MECs on the stiff PA-gels, as well as in MECs plated on the soft PA-gels exposed to hyperglycemia (Fig. 2B) and the coordinated decrease of the extracellular pH (pH_e) (Fig 2C). The reduced pH_e could be reversed by inhibiting the activity of ROCK or SLC9A1 (Fig. 2C), a ROCK regulated ion channel also known as Na^+/H^+ Exchanger 1 (NHE1). Inhibition of SLC9A1 with BIX or EIPA also restored mitochondrial morphology in MECs plated on stiff PA-gels to the filamentous morphology exhibited by MECs plated on soft PA-gels (Fig. 2D & S2A). SLC9A1 inhibition restored the concentrations of approximately 60% of the significantly altered metabolites we measured in MECs plated on the stiff PA-gels back to the concentrations observed in MECs on soft PA-gels (Fig. 2E). SLC9A1 inhibition also rescued the impaired mitochondrial respiration caused by adhesion-induced or ROCK-increased cell tension (Fig. S2B-C-D). CRISPR-mediated knockout of SLC9A1 in MECs (*SLC9A1-KO*) resulted in MECs that maintained a filamentous mitochondrial morphology on stiff PA-gels (Fig. 2F). *SLC9A1-KO* was also sufficient to normalize mitochondrial respiration in MECs exposed to hyperglycemia, as well as those with high adhesion-dependent cytoskeletal tension induced by plating on a high-density fibronectin (Fig. S2F-G).

To explore the physiological relevance of our findings, we next tested the ability of SLC9A1 to affect mitochondrial morphology in C. elegans, a model organism that is amenable to live microscopy of mitochondria and genetic manipulations (*22*) and that has been used extensively to study OxSR (*23*). RNAi-mediated knockdown of *nhx-2* (*SLC9A1* orthologue) prevented the mitochondrial fragmentation or toroidal phenotype typically found in the aged gut epithelium of this organism (Fig. 2G). These findings corroborate the *in vitro* evidence that the toroidal mitochondrial structures induced by cytoskeletal tension may reflect an adaptive phenotype mediated by *SLC9A1*.

In addition to pH regulation, SLC9A1 facilitates Na^+ import that reverses the directionality of the Na^+/Ca^{2+} exchangers (NCX, SLC8A1-3), a process which causes mitochondrial ROS production *via* mitochondrial calcium overload (*24, 25*). To determine if adhesion-dependent cytoskeletal tension regulates mitochondrial calcium content through SLC9A1 activity, we measured mitochondrial and total cellular calcium levels in MECs plated on soft versus stiff PA-gels. Imaging of Rhod2-AM and Calcium Green-1 AM revealed that mitochondrial calcium concentration was highest on the stiff PA-gels,

and could be reduced either by inhibiting or knocking out SLC9A1 (Fig. 3A). Consistently, treating cells with CGP37157 or kaempferol, to increase mitochondrial calcium load, induced the toroidal/fragmented mitochondrial morphology in MECs plated on the soft PA-gels (Fig. 3B). Suppression of mitochondrial ROS, with MitoTempo, or the mitochondrial calcium loading *via* inhibition of NCX, with SN-6, and the mitochondrial calcium uniporter (MCU), with ru360, prevented toroid formation on stiff PA-gels (Fig. S3A). Furthermore, SLC9A1 inhibition was able to suppress the mitochondrial ROS induced by mitochondrial calcium loading in the CGP37157-treated cells on the soft PA-gels (Fig. S3B). These data indicate that SLC9A1 activity influences mitochondrial calcium concentration and ROS signals that may serve to activate an OxSR adaptation through the formation of toroidal mitochondria.

Sub-lethal stresses can induce cellular stress responses that protect cells from future or greater insults through adaptive transcription and translation (e.g. ROS promotes OxSR *via* NRF2 activation (*26*)). Mitochondrial stress, particularly ROS production and respiratory dysfunction, promote adaptive reprogramming of mitochondrial function through a process described as "mitohormesis" (*27*). Consistent with a relationship between SLC9A1 activity (nhx-2 activity) and ROS production, *nhx-2* (*SLC9A1*) knockdown reduced expression of an oxidative stress reporter (GST4:GFP fusion protein) (Fig. 3C), which primarily reports on the activity of *skn-1* (*NRF-2* orthologue). As a positive control, we treated the oxidative stress reporter animals with paraquat, a herbicide that promotes mitochondrial ROS leak/production (*28*). While control animals showed the expected increase in oxidative stress reporter activity, the *nhx-2* knockdown worms were much more sensitive to oxidative stress than control animals (Fig. 3C). To confirm the role of *nhx-2* and oxidative stress sensitivity, we challenged these worms with a higher dose of paraquat and assayed survival. Indeed, *nhx-2* knockdown rendered these animals much more sensitive to paraquat-induced death (Fig. 3D). We interpreted these data to indicate the *nhx-2* animals experienced lower levels of mitochondrial ROS mediated damage, and therefore were not adapted to survive the paraquat challenge. ROS-mediated damage/signaling not only regulates pathologies such as cardiovascular disease but also can significantly alter lifespan (*23, 29*). In agreement with the free radical theory of ageing, we found that the lifespan of the C. elegans *nhx-2* knockdown was dramatically extended (Fig. S3C). Accordingly, these results indicate that SLC9A1-activity induces OxSR *via* sub-lethal mitochondrial ROS which promotes mitochondrial reorganization (toroid formation).

Cytoskeletal tension activates HSF1-mediated mitochondrial reprogramming

We next utilized RNA-Seq to identify molecules that could mediate the cytoskeletal tension-induced alterations in mitochondrial structure/function and OxSR adaptation (Fig. 4A). We compared the transcriptional programs induced by hyperglycemia and adhesion substrate elasticity because they both induce cytoskeletal tension, trigger mitochondrial reorganization (toroid formation), and alter mitochondrial respiration. Unsupervised hierarchical clustering determined that the greatest transcriptomic signature overlap occurred in MECs plated on the soft PA-gels (400 Pa) that were exposed to hyperglycemia [25 mM] and MECs plated on the stiff PA-gels (60k Pa) with physiological glucose [5 mM]. Gene ontology revealed that many genes associated with epithelial cell differentiation were downregulated in both conditions of high cytoskeletal tension.

Moreover, a number of mitochondrial electron transport chain (ETC) subunits were also downregulated including (*NDUFA7, ATP5B, ATP5D, COX6b1* etc.). In addition to the expected up regulated genes linked to cytoskeletal remodeling, DNA damage repair, cell cycle regulation, and organelle inheritance (Fig. S4A-B), we found upregulation of multiple mitochondrial-localized chaperones and proteases, which facilitate mitochondrial import, protein folding, and structural remodeling of the mitochondria during UPR^mt (*YME1L1, HSPE1, DNAJC10 (hsp40)), HSPD1, HSPA9, HSPB11,* etc.). However, the gene expression data indicated that stiff PA-gels or hyperglycemia caused HSP/chaperone induction more reminiscent of a HSF1-mediated heat-shock response than the canonical UPR^mt (*30*).

HSF1 regulates a transcription program that promotes the survival of cells experiencing heat stress (~43ºC). HSF1 can also induce a heat-stress independent transcriptional program implicated in cancer (*31*), and was induced in MECs plated on stiff PA-gels or exposed to hyperglycemia (Fig. 4A-4B, & S4C). Inhibiting cytoskeletal tension (Y27632) or SLC9A1 in MECs with high cytoskeletal tension and toroidal mitochondria not only normalized their metabolic state, but also repressed the expression of HSF1 and its downstream targets (Fig. S4D). A causal link between HSF1 and toroid-associated mitochondrial metabolic adaptation was further supported by experiments showing that inhibition of HSF1, with KRIBB11, permitted the formation of thin filamentous "normalized" or "non-stress adapted" mitochondrial networks on stiff PA-gels (Fig. 4C). Inhibition of HSF1 restored ~80% of the metabolite concentrations measured in MECs plated on stiff PA-gels to that of MECs on soft PA-gels (Fig. 4D). These findings suggest cytoskeletal tension stimulates mitochondrial reorganization and metabolic reprogramming by activating a heat-stress independent HSF1 transcription program (*31*).

HSF1 could modify mitochondrial structure/function by influencing the expression of components of the mitochondrial import machinery, such as mtHSP70 (*HSPA9*) (*32*), or by regulating mitochondrial biogenesis in collaboration with peroxisome proliferator-activated receptor gamma coactivator 1-alpha (PGC-1α) (*33*). Consistent with both paradigms, we used stable isotope incorporation mass spectrometry, which monitors the incorporation of newly synthesized proteins into the mitochondria, which revealed that cytoskeletal tension increased mitochondrial protein turnover rates. HSF1 inhibition was sufficient to prevent cytoskeletal tension increased mitochondrial protein turnover (Fig. 4E). The findings indicate that HSF1 plays a critical role in managing mitochondrial structure/function by regulating mitochondrial biogenesis/protein-turnover.

To explore how cytoskeletal tension elicits HSF1-dependent OxSR, we quantified the levels of reduced and oxidized glutathione, the primary cellular oxidant detoxification and redox (reduction:oxidation) management system which becomes oxidized in the presence of ROS. MECs on the stiff PA-gels had lower levels of oxidized glutathione than MECs on soft Pa-gels (Fig. 4F). HSF1 inhibition was sufficient to significantly increase the levels of oxidized glutathione in MECs on stiff PA-gels (Fig.4F). Metabolomics allowed us to observe that many metabolite changes that reflect OxSR (*34*), and pentose phosphate pathway activity, which generates reduced nicotinamide adenine dinucleotide phosphate (NADPH) required to regenerate reduced glutathione and mitigate oxidative stress, were also elevated in response to cytoskeletal tension, and could be normalized

by inhibiting HSF1 transcriptional activity (Fig. S4E). Indeed, we noted that HSF1 inhibition abolished the reducing capacity of MECs plated on stiff PA-gels (Fig. 4G). These data led us to speculate that the OxSR could be due to HSF1-dependent changes in cellular metabolism facilitated by mitochondrial proteome turnover, which mediate metabolic reprogramming *via* adjustments to the mitochondrial proteome composition (Fig. 4D-E).

To further implicate HSF1 in mitochondrial reorganization and OxSR adaptation we pharmacologically activated HSF1 using Celastrol, a reactive electrophile derived from the "Thunder of God" vine (Tripterygium wilfordii) (*35*). Celastrol treatment induced mitochondrial fragmentation/toroids in MECs plated on the soft PA-gels such that their morphology was comparable to those found in MECs with high cytoskeletal tension (60k Pa; 5 mM glucose or 400 Pa; 25 mM glucose; Fig. 5A & S5A). HSF1 activation also increased extracellular acidification (ECAR), a proxy measure of glycolytic flux, and reduced mitochondrial oxygen consumption (Fig. 5B). A mitochondria-localized ROS reporter (MitoPY1) revealed that MECs treated with Celastrol had significantly suppressed mitochondrial ROS levels (Fig. S5B). Moreover, expression of constitutively active HSF1 similarly induced toroid mitochondria in MECs plated on the soft PA-gels (Fig. S5C), and increased mitochondrial membrane potential (Fig. S5D). Conversely, HSF1 knockdown increased mitochondrial respiration (Fig. 5C), induced oxidative stress (Fig. 5D & S5E), and decreased mitochondrial membrane potential (Fig. 5E & S5F) in both the MCF10A (nonmalignant) and MDA-MB-231 (aggressive and malignant) MECs (Fig. S5G-J). The physiological relevance of the findings was confirmed by showing that reducing *hsf-1* expression in C. elegans both decreased mitochondrial mass as well as membrane potential throughout the whole organism (Fig. 5D-E). Accordingly, the findings indicate HSF1 activity is a master regulator of stress-dependent mitochondrial structure/function adaptation.

Cytoskeletal tension engenders mitochondrial OxSR *via* HSF1 and YME1L1

Thus far, our data suggest that cytoskeletal tension stimulates a heat-stress independent HSF1 transcriptional program, previously implicated in cancer, that drives mitochondrial toroid formation, and restricts mitochondrial respiration and oxidant production. Accordingly, we next tested if this OxSR adaption was sufficient to oppose ROS mediated apoptosis, a trait associated with many tumors (*36*). We treated MECs with high or low cytoskeletal tension, with paraquat, a mitochondrial redox cycler that promotes superoxide (O^-_2) and hydrogen peroxide (H_2O_2) leak/generation from the mitochondria, and assayed for apoptosis (*16*). Consistent with the hypothesis that cytoskeletal tension promotes OxSR *via* HSF1, MECs cultured on stiff PA-gels were less sensitive to paraquat treatment. This OxSR phenotype could be further enhanced *via* expression of constitutively active HSF1 and ablated by HSF1 knockdown or inhibition (Fig. 6A-B & S6A-B). Functional links between cytoskeletal tension and mitochondrial OxSR adaptation were verified by determining that mitochondrial depletion negated the impact of ECM stiffness on cellular redox sensitivity to paraquat (Fig. S6B).

Due to the fact that cytoskeletal tension altered mitochondrial protein turnover rates, and mitochondrial import is required for mitochondrial protein turnover, we decided to test if cytoskeletal tension mediated OxSR was dependent on mitochondrial protein import. Nuclear-encoded mitochondrial proteins are imported into the mitochondria (*37*),

a process which requires a number HSF1 target genes to efficiently occur (e.g. *HSPD1* (HSP60), *HSPE1* (HSP10), and *HSPA9* (mtHSP70) (*38*, *39*). To test if cytoskeletal tension enhanced mitochondrial import was critical for OxSR, we used JG-98, an inhibitor of HSP70 that enriches in mitochondria (*40*, *41*). JG-98 treated cells grown in stiff environments were not spontaneously apoptotic, but were sensititized to paraquat-induced death (Fig. 6C).

To identify the specific mediators of the HSF1-dependent OxSR we cross-referenced conserved nuclear-encoded mitochondrial genes containing heat-shock elements (HSE) in their promoters with genes whose expression was upregulated by cytoskeletal tension (Fig. 3A). We found one likely candidate, mitochondrial escape 1 like 1 (*YME1L1*), a zinc-dependent metalloprotease of the AAA$^+$ protein family (ATPases with diverse cellular activity), which is associated with UPR^{mt} and mitochondrial morphology management (*42*, *43*). We verified that YME1L1 protein levels were regulated by HSF1 and were upregulated by increasing cytoskeletal tension (Fig. 6D-E). To test if HSF1 activity conferred OxSR through YME1L1 abundance, we examined the paraquat sensitivity of *hsf-1*-overexpressing C. elegans with or without reduced expression of *yme-1* (*YME1L1* orthologue). As expected, overexpression of *hsf-1* rendered C. elegans more resistant to paraquat-induced death, to a greater extent than that observed in other long lived strains (e.g. daf-2 knockdown). Impressively, *yme-1* knockdown completely abolished the OxSR conferred to C. elegans through the overexpression of HSF1.

Discussion

We identified a mechanism whereby cytoskeletal tension regulates mitochondrial composition, structure and function to tune cellular metabolism through stress adaptation. We demonstrated that SLC9A1 and HSF1-mediated alterations in mitochondrial function support OxSR by increasing mitochondrial protein turnover and limiting respiration, likely through the proteolytic activity of YME1L1 (*43*). The mechano-responsiveness of HSF1 and its ability to limit mitochondrial respiration, may explain why oncogene driven Warburg metabolism has been so difficult to observe *in vitro*. The rigid tissue culture polystyrene substrates (3G Pa) elevates cytoskeletal tension and chronically activates HSF1, regardless of oncogene-transformation, and this effect obscures any comparative measurements of mitochondrial function in normal and oncogene-transformed cells. Instead, prudent use of model systems with biomimetic properties (physically and chemically similar to the relevant biological system) are needed to uncover oncogene driven alterations in mitochondrial metabolism (*44*, *45*).

Our findings demonstrate that HSF1-driven redox management not only suppresses the production of ROS, by limiting mitochondrial respiration, but it also opposes oxidant damage by promoting mitochondrial biogenesis/protein turnover and enhancing reducing equivalents (glutathione/NADPH). Previous studies have indicated that cell-detachment/attachment-associated signaling elicits redox stress (*46–48*). With that in mind, coupling redox stress management to a molecular rheostat would be a rational design principle. HSF1 is a logical candidate to serve as such a molecular rheostat. If HSF1 is such a molecular rheostat it would become transcriptionally active when misfolded proteins accumulate. Misfolded proteins can accumulate due to changes in pH, ion concentrations, osmolality, osmotic pressure, molecular crowding, adhesion associated compressive forces, enthalpy (heat), entropy (order), and redox balance (*49–*

53) all cellular conditions associated with HSF1 activation. By surveying the physical state of the proteome, HSF1 is well poised to temper diverse environmental perturbations that elicit mitochondrial dysfunction and oxidant leak. Indeed, HSF1 could mitigate the redox stress induced by conditions that deform mitochondrial structure (*3*), such as the physical stresses cells encounter in tumors with high interstitial pressure, mechanically stressful metastatic sites (*54*), rigid ECMs, or oncogene induced ROCK activity (*55–57*).

HSF1 levels are elevated in the majority of tumors and has been implicated in cancer aggression and metastasis (*31, 58, 59*). Because tumors are stiffer and the tumor cell has higher cytoskeletal tension, our findings offer a tractable explanation for why HSF1 and its target genes are so frequently upregulated in these tissues (*60*). The heat shock independent activation of HSF1 and its target genes would provide the tumor cells with a metabolic adaptation to this chronic mechanical stress (Fig. S6D-E). In this regard, therapeutic approaches to disrupt HSF1 and its target genes have focused on cytosolic and nuclear targets that showed promise in preclinical models, but can incur difficult to tolerate systemic effects in humans (*61*). Our data implicate the mitochondrial protease YME1L1 as a HSF1 target gene that facilitates stress adaptation, suggesting alternative, potentially less toxic targets might exist. Our findings support the notion that pharmacological inhibition of the HSF1-mediated mitochondrial reprogramming may be an effective anti-tumor therapeutic strategy (*43*).

References:
1.   J. S. Park, C. J. Burckhardt, R. Lazcano, L. M. Solis, T. Isogai, L. Li, C. S. Chen, B. Gao, J. D. Minna, R. Bachoo, R. J. DeBerardinis, G. Danuser, *Nature*, in press, doi:10.1038/s41586-020-1998-1.
2.   V. Papalazarou, T. Zhang, N. R. Paul, A. Juin, M. Cantini, O. D. K. Maddocks, M. Salmeron-Sanchez, L. M. Machesky, The creatine–phosphagen system is mechanoresponsive in pancreatic adenocarcinoma and fuels invasion and metastasis. *Nat. Metab.* **2**, 62–80 (2020).
3.   S. C. J. Helle, Q. Feng, M. J. Aebersold, L. Hirt, R. R. Grüter, A. Vahid, A. Sirianni, S. Mostowy, J. G. Snedeker, A. Šarić, T. Idema, T. Zambelli, B. Kornmann, Mechanical force induces mitochondrial fission. *Elife*. **6**, e30292 (2017).
4.   U. Manor, S. Bartholomew, G. Golani, E. Christenson, M. Kozlov, H. Higgs, J. Spudich, J. Lippincott-Schwartz, A mitochondria-anchored isoform of the actin-nucleating spire protein regulates mitochondrial division. *Elife*. **4**, e08828 (2015).
5.   A. S. Moore, Y. C. Wong, C. L. Simpson, E. L. F. Holzbaur, Dynamic actin cycling through mitochondrial subpopulations locally regulates the fission-fusion balance within mitochondrial networks. *Nat. Commun.* **7**, 12886 (2016).
6.   S. R. Caliari, J. A. Burdick, A practical guide to hydrogels for cell culture. *Nat. Methods*. **13**, 405–414 (2016).
7.   K. M. Tharp, V. M. Weaver, Modeling Tissue Polarity in Context. *J. Mol. Biol.* **430**, 3613–3628 (2018).
8.   D. T. Butcher, T. Alliston, V. M. Weaver, A tense situation: forcing tumour progression. *Nat. Rev. Cancer*. **9**, 108–122 (2009).
9.   M. J. Paszek, N. Zahir, K. R. Johnson, J. N. Lakins, G. I. Rozenberg, A. Gefen, C. A. Reinhart-King, S. S. Margulies, M. Dembo, D. Boettiger, D. A. Hammer, V. M. Weaver, Tensional homeostasis and the malignant phenotype. *Cancer Cell*. **8**, 241–254 (2005).
10.   R. Oria, T. Wiegand, J. Escribano, A. Elosegui-Artola, J. J. Uriarte, C. Moreno-Pulido, I. Platzman, P. Delcanale, L. Albertazzi, D. Navajas, X. Trepat, J. M. García-Aznar, E. A.

Cavalcanti-Adam, P. Roca-Cusachs, Force loading explains spatial sensing of ligands by cells. *Nature*. **552**, 219–224 (2017).

11. G. L. Lin, D. M. Cohen, R. A. Desai, M. T. Breckenridge, L. Gao, M. J. Humphries, C. S. Chen, Activation of beta 1 but not beta 3 integrin increases cell traction forces. *FEBS Lett.* **587**, 763–769 (2013).

12. D. R. Croft, M. F. Olson, Conditional regulation of a ROCK-estrogen receptor fusion protein. *Methods Enzymol.* **406**, 541–553 (2006).

13. Q. Wang, M. Zhang, G. Torres, S. Wu, C. Ouyang, Z. Xie, M.-H. Zou, Metformin Suppresses Diabetes-Accelerated Atherosclerosis via the Inhibition of Drp1-Mediated Mitochondrial Fission. *Diabetes*. **66**, 193–205 (2017).

14. B.-C. Chen, W. R. Legant, K. Wang, L. Shao, D. E. Milkie, M. W. Davidson, C. Janetopoulos, X. S. Wu, J. A. Hammer 3rd, Z. Liu, B. P. English, Y. Mimori-Kiyosue, D. P. Romero, A. T. Ritter, J. Lippincott-Schwartz, L. Fritz-Laylin, R. D. Mullins, D. M. Mitchell, J. N. Bembenek, A.-C. Reymann, R. Böhme, S. W. Grill, J. T. Wang, G. Seydoux, U. S. Tulu, D. P. Kiehart, E. Betzig, Lattice light-sheet microscopy: imaging molecules to embryos at high spatiotemporal resolution. *Science*. **346**, 1257998 (2014).

15. J. E. Aldridge, T. Horibe, N. J. Hoogenraad, Discovery of genes activated by the mitochondrial unfolded protein response (mtUPR) and cognate promoter elements. *PLoS One*. **2**, e874–e874 (2007).

16. H.-G. Sprenger, T. Langer, The Good and the Bad of Mitochondrial Breakups. *Trends Cell Biol.* **29**, 888–900 (2019).

17. G. Twig, O. S. Shirihai, The interplay between mitochondrial dynamics and mitophagy. *Antioxid. Redox Signal.* **14**, 1939–1951 (2011).

18. Y. Miyazono, S. Hirashima, N. Ishihara, J. Kusukawa, K.-I. Nakamura, K. Ohta, Uncoupled mitochondria quickly shorten along their long axis to form indented spheroids, instead of rings, in a fission-independent manner. *Sci. Rep.* **8**, 350 (2018).

19. X. Liu, G. Hajnóczky, Altered fusion dynamics underlie unique morphological changes in mitochondria during hypoxia-reoxygenation stress. *Cell Death Differ.* **18**, 1561–1572 (2011).

20. P. Lindström, J. Sehlin, Effect of glucose on the intracellular pH of pancreatic islet cells. *Biochem. J.* **218**, 887–892 (1984).

21. T. Tominaga, T. Ishizaki, S. Narumiya, D. L. Barber, p160ROCK mediates RhoA activation of Na-H exchange. *EMBO J.* **17**, 4712–4722 (1998).

22. K. Nehrke, J. E. Melvin, The NHX family of Na+-H+ exchangers in Caenorhabditis elegans. *J. Biol. Chem.* **277**, 29036–29044 (2002).

23. M. Ristow, S. Schmeisser, Extending life span by increasing oxidative stress. *Free Radic. Biol. Med.* **51**, 327–336 (2011).

24. P. S. Brookes, Y. Yoon, J. L. Robotham, M. W. Anders, S.-S. Sheu, Calcium, ATP, and ROS: a mitochondrial love-hate triangle. *Am. J. Physiol. Cell Physiol.* **287**, C817–C833 (2004).

25. C. Giorgi, S. Marchi, P. Pinton, The machineries, regulation and cellular functions of mitochondrial calcium. *Nat. Rev. Mol. Cell Biol.* **19**, 713–730 (2018).

26. Q. Ma, Role of nrf2 in oxidative stress and toxicity. *Annu. Rev. Pharmacol. Toxicol.* **53**, 401–426 (2013).

27. M. Ristow, Unraveling the truth about antioxidants: mitohormesis explains ROS-induced health benefits. *Nat. Med.* **20**, 709–711 (2014).

28. P. R. Castello, D. A. Drechsel, M. Patel, Mitochondria are a major source of paraquat-induced reactive oxygen species production in the brain. *J. Biol. Chem.* **282**, 14186–14193 (2007).

29. K. B. Beckman, B. N. Ames, The free radical theory of aging matures. *Physiol. Rev.* **78**, 547–581 (1998).

30. J. Labbadia, R. M. Brielmann, M. F. Neto, Y.-F. Lin, C. M. Haynes, R. I. Morimoto, Mitochondrial Stress Restores the Heat Shock Response and Prevents Proteostasis Collapse during Aging. *Cell Rep.* **21**, 1481–1494 (2017).

31. M. L. Mendillo, S. Santagata, M. Koeva, G. W. Bell, R. Hu, R. M. Tamimi, E. Fraenkel, T. A. Ince, L. Whitesell, S. Lindquist, HSF1 drives a transcriptional program distinct from heat shock to support highly malignant human cancers. *Cell*. **150**, 549–562 (2012).

32. N. Wiedemann, N. Pfanner, Mitochondrial Machineries for Protein Import and Assembly. *Annu. Rev. Biochem.* **86**, 685–714 (2017).

33. A. E. Charos, B. D. Reed, D. Raha, A. M. Szekely, S. M. Weissman, M. Snyder, A highly integrated and complex PPARGC1A transcription factor binding network in HepG2 cells. *Genome Res.* **22**, 1668–1679 (2012).

34. S. E. LeBoeuf, W. L. Wu, T. R. Karakousi, B. Karadal, S. R. Jackson, S. M. Davidson, K.-K. Wong, S. B. Koralov, V. I. Sayin, T. Papagiannakopoulos, Activation of Oxidative Stress Response in Cancer Generates a Druggable Dependency on Exogenous Non-essential Amino Acids. *Cell Metab.* **31**, 339-350.e4 (2020).

35. X. Ma, L. Xu, A. T. Alberobello, O. Gavrilova, A. Bagattin, M. Skarulis, J. Liu, T. Finkel, E. Mueller, Celastrol Protects against Obesity and Metabolic Dysfunction through Activation of a HSF1-PGC1α Transcriptional Axis. *Cell Metab.* **22**, 695–708 (2015).

36. C. R. Reczek, K. Birsoy, H. Kong, I. Martínez-Reyes, T. Wang, P. Gao, D. M. Sabatini, N. S. Chandel, A CRISPR screen identifies a pathway required for paraquat-induced cell death. *Nat. Chem. Biol.* **13**, 1274–1279 (2017).

37. O. Schmidt, N. Pfanner, C. Meisinger, Mitochondrial protein import: from proteomics to functional mechanisms. *Nat. Rev. Mol. Cell Biol.* **11**, 655–667 (2010).

38. H. C. Schneider, J. Berthold, M. F. Bauer, K. Dietmeier, B. Guiard, M. Brunner, W. Neupert, Mitochondrial Hsp70/MIM44 complex facilitates protein import. *Nature*. **371**, 768–774 (1994).

39. C. C. Deocaris, S. C. Kaul, R. Wadhwa, On the brotherhood of the mitochondrial chaperones mortalin and heat shock protein 60. *Cell Stress Chaperones*. **11**, 116–128 (2006).

40. X. Li, S. R. Srinivasan, J. Connarn, A. Ahmad, Z. T. Young, A. M. Kabza, E. R. P. Zuiderweg, D. Sun, J. E. Gestwicki, Analogs of the Allosteric Heat Shock Protein 70 (Hsp70) Inhibitor, MKT-077, as Anti-Cancer Agents. *ACS Med. Chem. Lett.* **4**, 1042–1047 (2013).

41. S. R. Srinivasan, L. C. Cesa, X. Li, O. Julien, M. Zhuang, H. Shao, J. Chung, I. Maillard, J. A. Wells, C. S. Duckett, J. E. Gestwicki, Heat Shock Protein 70 (Hsp70) Suppresses RIP1-Dependent Apoptotic and Necroptotic Cascades. *Mol. Cancer Res.* **16**, 58–68 (2018).

42. T. MacVicar, T. Langer, OPA1 processing in cell death and disease - the long and short of it. *J. Cell Sci.* **129**, 2297–2306 (2016).

43. T. MacVicar, Y. Ohba, H. Nolte, F. C. Mayer, T. Tatsuta, H.-G. Sprenger, B. Lindner, Y. Zhao, J. Li, C. Bruns, M. Krüger, M. Habich, J. Riemer, R. Schwarzer, M. Pasparakis, S. Henschke, J. C. Brüning, N. Zamboni, T. Langer, Lipid signalling drives proteolytic rewiring of mitochondria by YME1L. *Nature*. **575**, 361–365 (2019).

44. J. R. Cantor, M. Abu-Remaileh, N. Kanarek, E. Freinkman, X. Gao, A. Louissaint Jr, C. A. Lewis, D. M. Sabatini, Physiologic Medium Rewires Cellular Metabolism and Reveals Uric Acid as an Endogenous Inhibitor of UMP Synthase. *Cell*. **169**, 258-272.e17 (2017).

45. P. DelNero, B. D. Hopkins, L. C. Cantley, C. Fischbach, Cancer metabolism gets physical. *Sci. Transl. Med.* **10**, eaaq1011 (2018).

46. Z. T. Schafer, A. R. Grassian, L. Song, Z. Jiang, Z. Gerhart-Hines, H. Y. Irie, S. Gao, P. Puigserver, J. S. Brugge, Antioxidant and oncogene rescue of metabolic defects caused by loss of matrix attachment. *Nature*. **461**, 109–113 (2009).

47. E. Werner, Z. Werb, Integrins engage mitochondrial function for signal transduction by a mechanism dependent on Rho GTPases. *J. Cell Biol.* **158**, 357–368 (2002).

48. D. C. Radisky, D. D. Levy, L. E. Littlepage, H. Liu, C. M. Nelson, J. E. Fata, D. Leake, E. L. Godden, D. G. Albertson, M. A. Nieto, Z. Werb, M. J. Bissell, Rac1b and reactive oxygen species mediate MMP-3-induced EMT and genomic instability. *Nature.* **436**, 123–127 (2005).

49. K. A. Dill, Dominant forces in protein folding. *Biochemistry.* **29**, 7133–7155 (1990).

50. M. Guo, A. F. Pegoraro, A. Mao, E. H. Zhou, P. R. Arany, Y. Han, D. T. Burnette, M. H. Jensen, K. E. Kasza, J. R. Moore, F. C. Mackintosh, J. J. Fredberg, D. J. Mooney, J. Lippincott-Schwartz, D. A. Weitz, Cell volume change through water efflux impacts cell stiffness and stem cell fate. *Proc. Natl. Acad. Sci. U. S. A.* **114**, E8618–E8627 (2017).

51. K. A. Dill, J. L. MacCallum, The protein-folding problem, 50 years on. *Science.* **338**, 1042–1046 (2012).

52. R. Higuchi-Sanabria, P. A. Frankino, J. W. Paul 3rd, S. U. Tronnes, A. Dillin, A Futile Battle? Protein Quality Control and the Stress of Aging. *Dev. Cell.* **44**, 139–163 (2018).

53. S.-G. Ahn, D. J. Thiele, Redox regulation of mammalian heat shock factor 1 is essential for Hsp gene activation and protection from stress. *Genes Dev.* **17**, 516–528 (2003).

54. B. A. Hassell, G. Goyal, E. Lee, A. Sontheimer-Phelps, O. Levy, C. S. Chen, D. E. Ingber, Human Organ Chip Models Recapitulate Orthotopic Lung Cancer Growth, Therapeutic Responses, and Tumor Dormancy In Vitro. *Cell Rep.* **21**, 508–516 (2017).

55. J. Irianto, C. R. Pfeifer, R. R. Bennett, Y. Xia, I. L. Ivanovska, A. J. Liu, R. A. Greenberg, D. E. Discher, Nuclear constriction segregates mobile nuclear proteins away from chromatin. *Mol. Biol. Cell.* **27**, 4011–4020 (2016).

56. P. Isermann, J. Lammerding, Consequences of a tight squeeze: Nuclear envelope rupture and repair. *Nucleus.* **8**, 268–274 (2017).

57. M. S. Samuel, J. I. Lopez, E. J. McGhee, D. R. Croft, D. Strachan, P. Timpson, J. Munro, E. Schröder, J. Zhou, V. G. Brunton, N. Barker, H. Clevers, O. J. Sansom, K. I. Anderson, V. M. Weaver, M. F. Olson, Actomyosin-mediated cellular tension drives increased tissue stiffness and β-catenin activation to induce epidermal hyperplasia and tumor growth. *Cancer Cell.* **19**, 776–791 (2011).

58. S. Santagata, R. Hu, N. U. Lin, M. L. Mendillo, L. C. Collins, S. E. Hankinson, S. J. Schnitt, L. Whitesell, R. M. Tamimi, S. Lindquist, T. A. Ince, High levels of nuclear heat-shock factor 1 (HSF1) are associated with poor prognosis in breast cancer. *Proc. Natl. Acad. Sci. U. S. A.* **108**, 18378–18383 (2011).

59. R. Scherz-Shouval, S. Santagata, M. L. Mendillo, L. M. Sholl, I. Ben-Aharon, A. H. Beck, D. Dias-Santagata, M. Koeva, S. M. Stemmer, L. Whitesell, S. Lindquist, The reprogramming of tumor stroma by HSF1 is a potent enabler of malignancy. *Cell.* **158**, 564–578 (2014).

60. I. Acerbi, L. Cassereau, I. Dean, Q. Shi, A. Au, C. Park, Y. Y. Chen, J. Liphardt, E. S. Hwang, V. M. Weaver, Human breast cancer invasion and aggression correlates with ECM stiffening and immune cell infiltration. *Integr. Biol. (Camb).* **7**, 1120–1134 (2015).

61. C. Dai, S. B. Sampson, HSF1: Guardian of Proteostasis in Cancer. *Trends Cell Biol.* **26**, 17–28 (2016).

significantly improved the quality of the manuscript. Chris Phillart, maintained the cellular respirometer used in these studies. Brant Webster, generated the MTS-roGFP2 vector. Fui Boon Kai, acquired the ROCK:ER construct and generated the ROCK:ER stable cell line. Bram Piersma, provided dry Dutch humor, beneficial laboratory ambiance, and conversation critical to the development of this manuscript.

Author contributions: Conceptualization: K.M.T. and V.M.W. Methodology: K.M.T, R.H.S. G.T., C.G.C., B.F., V.M.W., & A.D. Investigation: K.M.T., R.H.S., G.T., C.G.C., B.F., C.S., J.M., C.S., J.R.D., S.S.M. Formal Analysis: K.M.T., R.H.S., G.T., B.F., C.S., J.M., C.S., J.R.D., S.S.M. Data curation: K.M.T. Funding acquisition: V.M.W., K.M.T, A.D., M.H., D.K.N., A.R.D., K.S., & J.G. Project administration: K.M.T. Resources: V.M.W., K.M.T, A.D., M.H., D.K.N., A.R.D., K.S., H.S., & J.G. Software: C.S. & P.F. Supervision: V.M.W., A.D., K.S., A.R.D., D.K.N., M.H., J.G. Validation: K.M.T., R.H.S., G.T., C.G.C, and C.S. Visualization: K.M.T. Writing – original draft: K.M.T. Writing – review & editing: V.M.W., K.M.T., A.R.D., J.R.D., R.H.S., G.T., C.G.C., J.M., C.S., S.S.M.

Competing interests: Authors declare no competing interests.

Data and materials availability: All data is available in the main text or the supplementary materials.

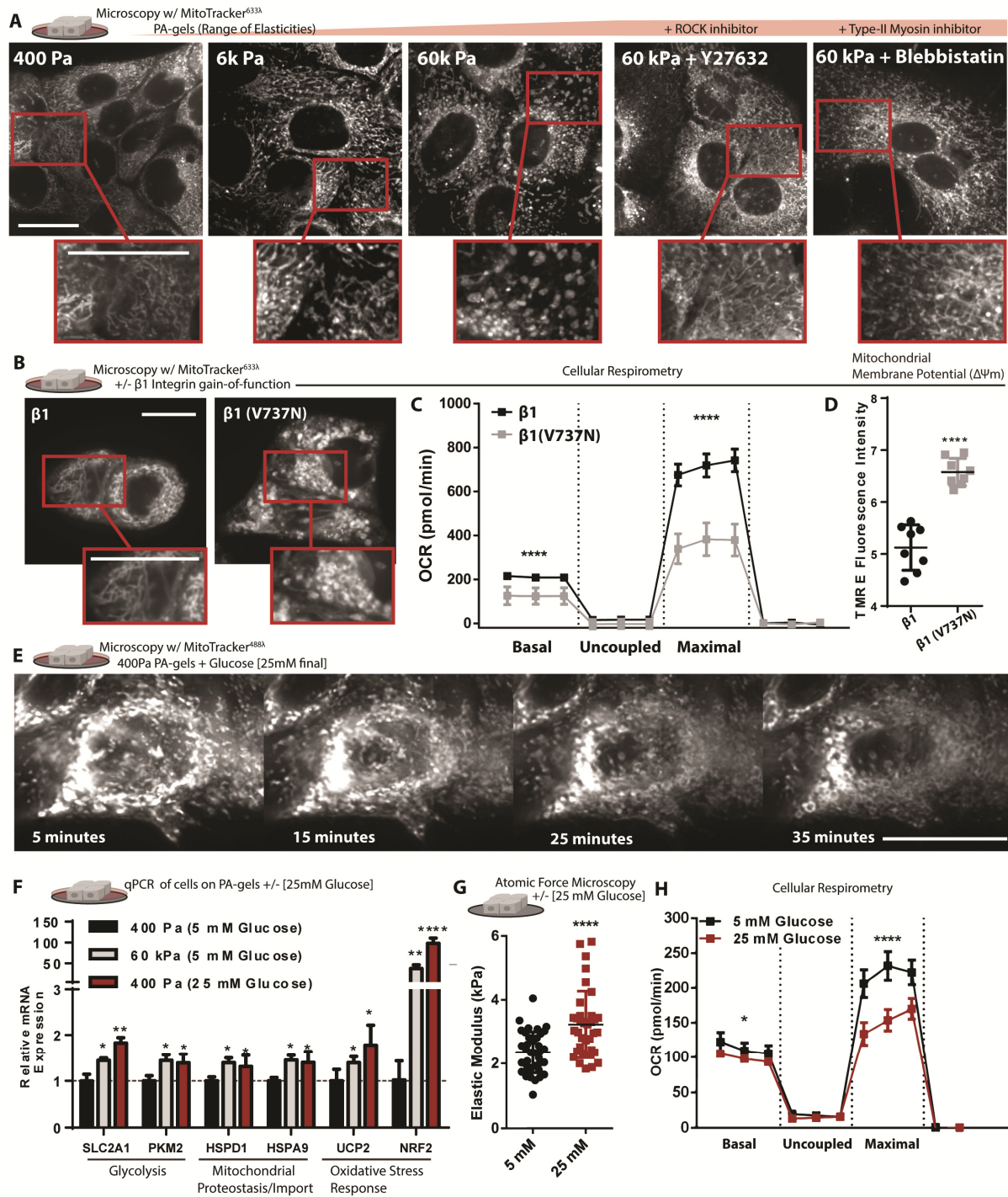**Supplementary Materials:** Materials and Methods and Figures S1-S6

Fig. 1. Cytoskeletal tension alters mitochondrial structure and function of human mammary epithelial cells (MECs).

A. Microscopy depicting mitochondrial network structure in cells cultured on varied elasticity polyacrylamide hydrogels (PA-gel) for 24 h, coated with fibronectin [6 µM/cm2] coating +/- y27632 [10 µM] or Blebbistatin [10 µM], stained with mitotracker (deep red FM) [100 nM].

B. Microscopy depicting mitochondrial network structure of β1-integrin or β1(V7373N) expressing cells cultured on 400 Pa surfaces for 24 h, stained with mitotracker (deep red FM) [100 nM].

C. Mitochondrial respiration, determined by oxygen consumption rate (OCR) of β1-integrin or β1(V7373N) expressing cells, (n=5 wells, 3 replicate measures), mitochondrial stress test conditions: uncoupled = oligomycin [1 µM], maximal = Trifluoromethoxy carbonylcyanide phenylhydrazone (FCCP) [1 µM], non-mitochondrial = antimycin A [1 µM] and rotenone [1 µM].

D. Mitochondrial membrane potential, measured after 1 h treatment of Tetramethylrhodamine ethyl-ester (TMRE) [10 nM] (n = 2 wells, repeated 4 times).

E. Representative microscopy of the mitochondrial network structure in live cells cultured in 5 mM glucose on 400 Pa PA-gels with a lattice light sheet microscope, monitoring structural changes after infusion of glucose [200 mM], rendering a final concentration of 25 mM glucose, mitotracker (Green FM) [100 nM].

F. Relative gene expression of MCF10A cells grown of varied stiffness PA-gels +/- glucose [25 mM] media normalized to 400 Pa surface with low glucose media [5 mM], qPCR-ΔΔCT (housekeeping gene: 18s) (n=5 or 4 separate experiments).

Data shown represents ± SEM. $*P < 0.05$, $**P < 0.01$, $***P < 0.005$, < 0.0001 *via* two-tailed unpaired Student t test in (C, D, F, G, and H).
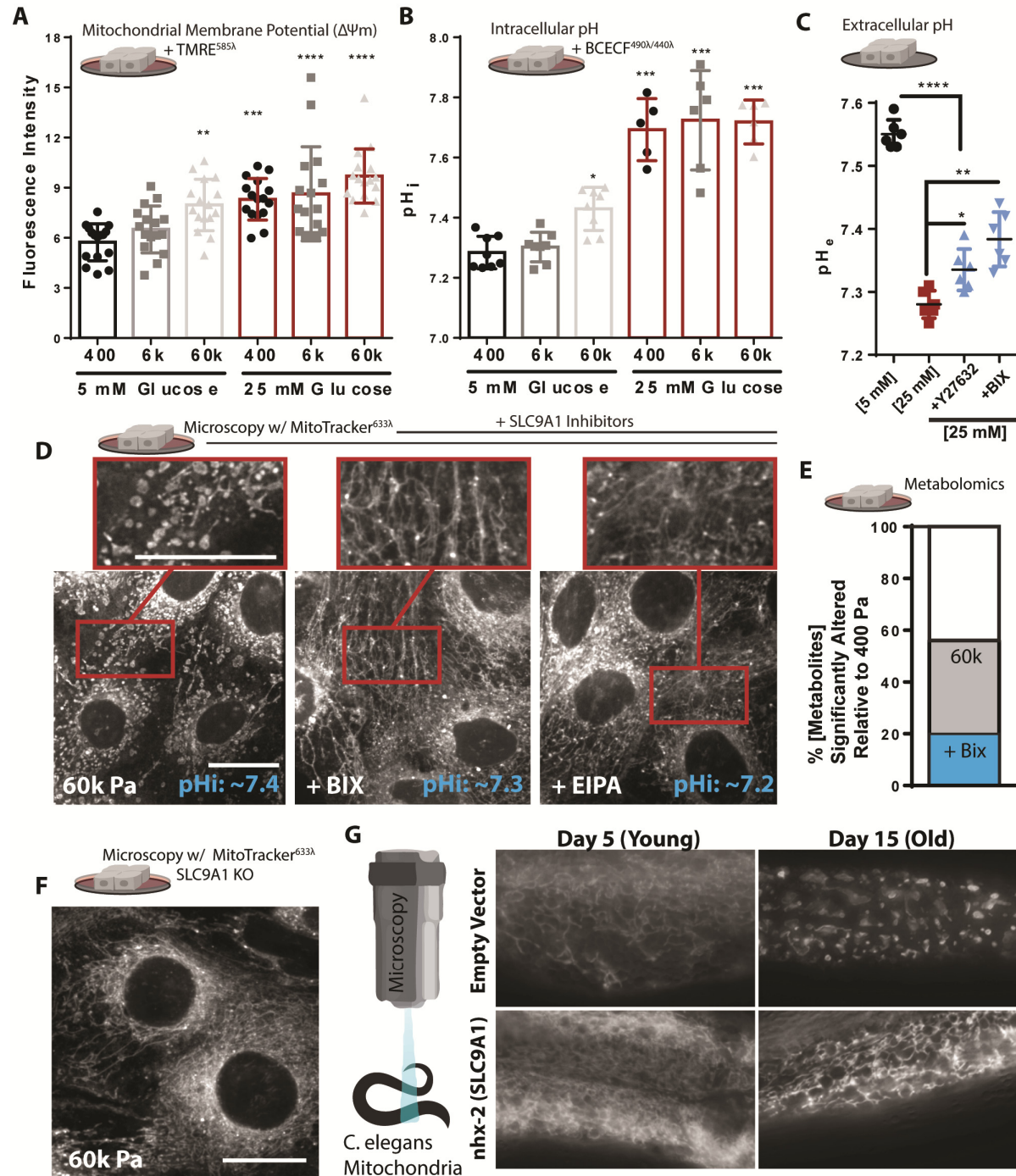
Fig. 2. SLC9A1 facilitates tension-mediated alterations in mitochondrial morphology and respiratory rate.

A. Mitochondrial membrane potential, measured after 1 h treatment of Tetramethylrhodamine ethyl-ester (TMRE) [10 nM] (n = 4 replicate PA gels repeated 4 times, shown together).

B. Intracellular pH (pHi) of cells grown of varied stiffness PA gels +/- glucose [25 mM], measured via 2',7'-Bis-(2-Carboxyethyl)-5-(and-6)-Carboxyfluorescein, Acetoxymethyl Ester (BCECF) [1 μM] (n=2 replicate PA gels repeated 3-4 times, shown together).

C. pH of media surrounding MCF10A cells cultured in glucose [5 or 25 mM] +/- DMSO, Y27632 [10 μM], or BIX [500 nM] with 200k cells/well of 12 well plate after 48 h (n=3 repeated twice, shown together).

D. Representative microscopy depicting mitochondrial network structure and caption depicting of pHi measurements of cells on 60k Pa surfaces treated with BIX [500 nM], EIPA [10 μM], or vehicle for 24 h, mitotracker (deep red FM) [100 nM] and BCECF [1 μM] (n=2 replicate PA gels repeated 3 times).

E. Metabolomics (LC-MS/MS) of cells cultured on PA-gels for 24h, % significantly altered relative to 400 Pa +/- BIX [500 nM]. (n=4-5 biological replicates LC-MS/MS run together, repeated twice)

F. Representative microscopy depicting mitochondrial network structure of *SLC9A1* KO cells on 60k Pa surfaces for 24 h, mitotracker (deep red FM) [100 nM].

G. Representative microscopy depicting mitochondrial network structure of live *C. elegans* expressing MLS::mRuby (mitochondrial matrix) grown on empty vector or *nhx-2* (*SLC9A1* orthologue) RNAi from hatch of 5 d or 15 d old animals.

Data shown represents ± SEM. *P < 0.05, **P < 0.01, ***P < 0.005, < 0.0001 *via* one-way ANOVA with Tukey test for multiple comparisons in (A, B, C, and E).
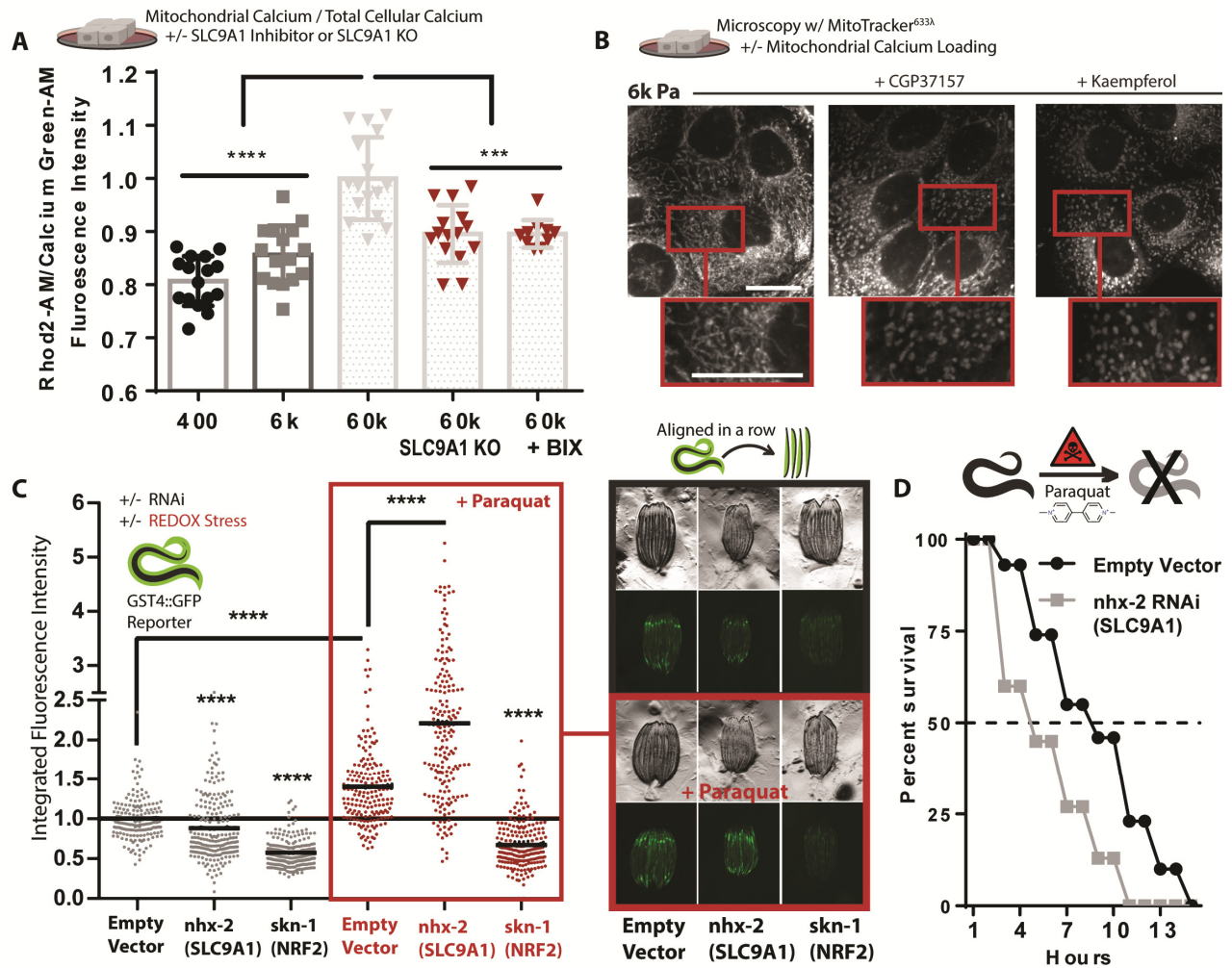
Fig. 3. SLC9A1 mediated mitochondrial calcium loading promotes oxidative stress and altered mitochondrial morphology.

A. Calcium content of MCF10A cells cultured on varied elasticity PA-gels for 24 h, treated with Rhod2-AM [2 µM] (mitochondrial) and Calcium Green-1-AM [2 µM] (intracellular). (n=4 replicates, repeated 4 times).

B. Representative microscopy depicting mitochondrial network structure of cells cultured on 6k Pa surfaces treated with CGP37157 [1 µM], kaempferol [10 µM], or vehicle for 1 h, mitotracker (deep red FM) [100 nM].

C. *gst-4p::GFP* reporter fluorescent intensity of *C.elegans* measured with a large particle cytometer, +/- paraquat [50 mM] (n=177, 206, 190, 187, 191, and 215 animals in order left to right) with representative images of *C.elegans* quantified.

D. *C. elegans* survival in 50 mM paraquat at 1 d; animals grown from hatch on on *nhx-2* RNAi vs empty-vector control (80 worms per condition).

Data shown represents ± SEM. *P < 0.05, **P < 0.01, ***P < 0.005, < 0.0001 *via* two-tailed unpaired Student t test in (D) and one-way ANOVA with Tukey test for multiple comparisons in (A and C).

bioRxiv "Preprint" Manuscript
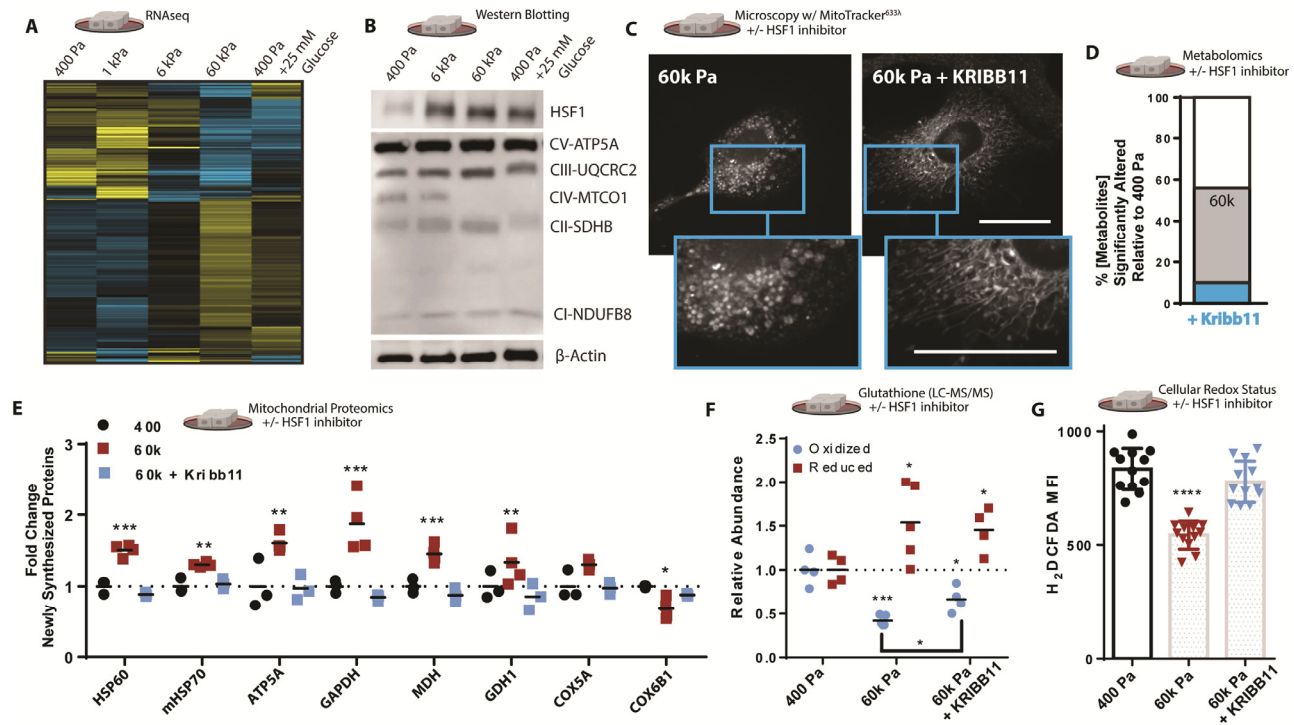
Figure 4: Cytoskeletal tension activates HSF1 *via* mitochondrial redox signals.

A. Heatmap depicting unsupervised hierarchical clustering of RNAseq of cells cultured on varied elasticity PA-gels for 24 h +/- glucose [5 or 25 mM], (n=2 duplicate libraries of 3 biological replicates, heatmap depicts mean of each condition, ~ 10 million reads per library).

B. Western blot depicting relative protein abundance of HSF1, electron transport chain components, or β-actin within 5 μg of total protein derived from lysates of cells cultured on varied elasticity PA-gels for 24 h +/- glucose [5 or 25 mM].

C. Representative microscopy of 100 nM mitotracker (deep red FM) stained and fixed (PFA) cells cultured on 60k Pa PA-gel surfaces for 24 h +/- vehicle or KRIBB11 [2 μM].

D. Metabolomics (LC-MS/MS) of cells cultured on PA-gels for 24h, % significantly altered relative to 400 Pa +/- KRIBB11 [2 μM]. (n=4-5 biological replicates LC-MS/MS run together, repeated twice)

E. Stable Isotope mitochondrial proteomics of crude mitochondrial fraction of MCF10A cells grown on PA-gels for 24h +/- KRIBB11 [2 μM] [(n=4 biological replicates LC-MS/MS run together, repeated twice)

F. Oxidized/reduced glutathione (NEM protected) measurements of MCF10A cells grown on PA-gels for 24h +/- KRIBB11 [2 μM] [(n=4 biological replicates, repeated twice) (n=4-5 biological replicates LC-MS/MS run together, repeated twice)

G. Oxidative stress indicator intensity of cells after 1 hour, MCF10A cells cultured on varied elasticity PA-gels for 24 h +/- vehicle or KRIBB11 [2 μM] prior, measured with 2',7'-dichlorodihydrofluorescein diacetate (H$_2$DCFDA) [2 μM].

Data shown represents ± SEM. *P < 0.05, **P < 0.01, ***P < 0.005, < 0.0001 *via* one-way ANOVA with Tukey test for multiple comparisons in (D, E, F, and G).
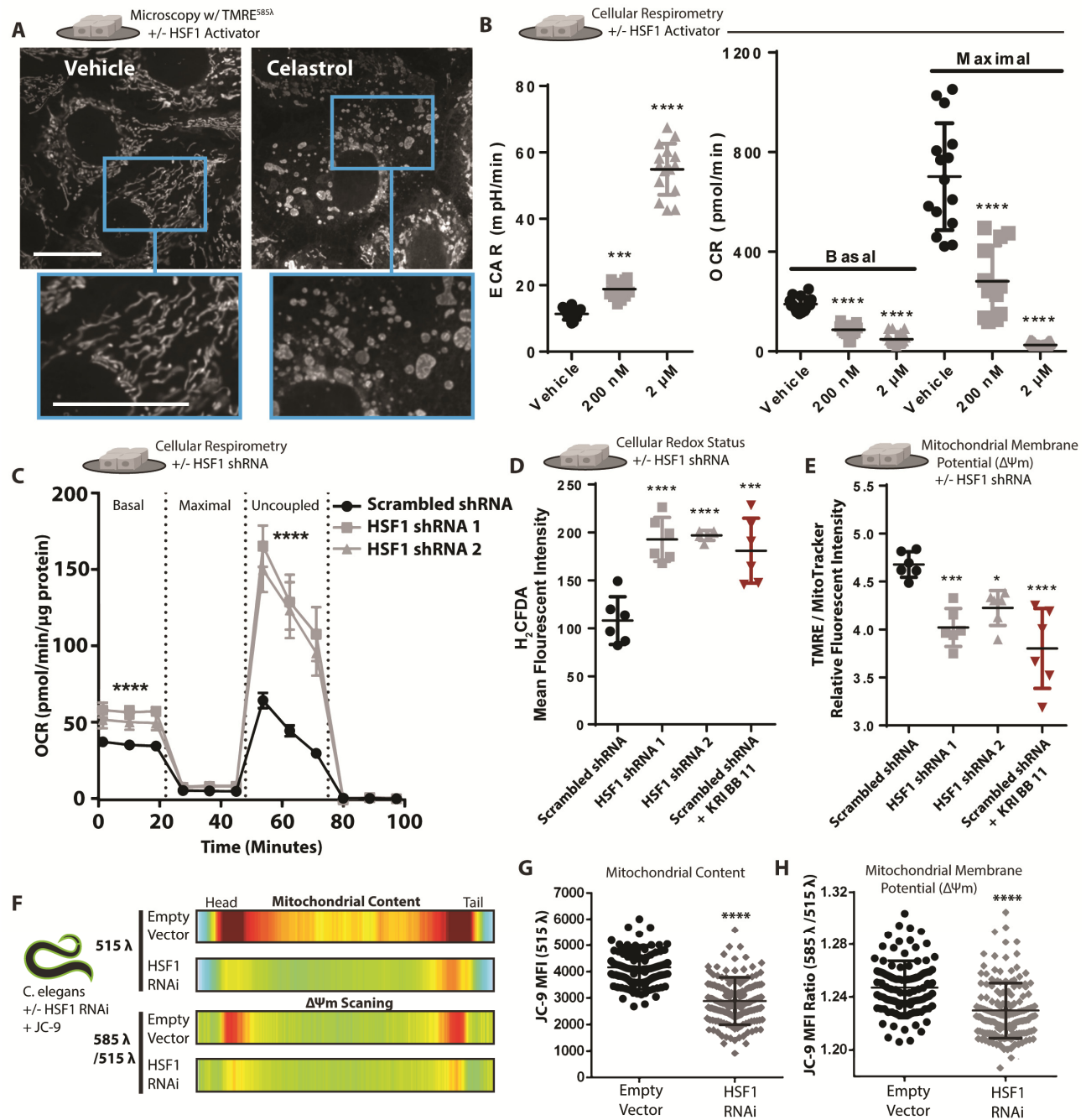
Figure 5: Cytoskeletal tension facilitates oxidative stress adaptation *via* HSF1 mediated mitochondrial reprogramming.

A. Representative microscopy depicting morphology and mitochondrial membrane potential staining of live cells *via* TMRE [10 nM] staining +/- vehicle or Celastrol [2 µM] treatment for 40 minutes prior to imaging.

B. Extracellular acidification rate (ECAR) and Oxygen consumption rate (OCR) of cells treated with +/- vehicle or Celastrol [200 nM] for 24 h or Celastrol [2 µM] for 40 minutes (n=5 wells, 3 replicate measures).

C. Oxygen consumption rate (OCR) of MCF10A cells expressing a scrambled shRNA or two different shRNAs targeting HSF1 (n=5 wells, repeated three times)

D. Oxidative stress indicator intensity after 1h in cells expressing a scrambled shRNA +/- KRIBB11 [2 µM] or two different shRNAs targeting HSF1, measured with 2',7'-dichlorodihydrofluorescein diacetate (H$_2$DCFDA) [2 µM]. (n=6 wells, repeated three times).

E. Mitochondrial membrane potential of MCF10A cells expressing a scrambled shRNA +/- KRIBB11 [2 µM] or two different shRNAs targeting HSF1, measured with TMRE [1 nM] and mitotracker [100nM] after 1 h staining (n=6, repeated three times).

F. Heatmap depicting mitochondrial mass (515 λ alone) or mitochondrial membrane potential (585 λ / 515 λ) across the body length (head (left) to tail (right)) of 150 *C. elegans* animals grown on empty vector or *hsf-1* RNAi from hatch; JC-9 staining *via* administration of JC-9 loaded *C.elegans* food (E.coli) (repeated three times).

G-H. Mean fluorescent intensity across the entire body length of the 150 animals spatially quantified in F.

Data shown represents ± SEM. *P < 0.05, **P < 0.01, ***P < 0.005, < 0.0001 *via* two-tailed unpaired Student t test in (C, G, and H) and one-way ANOVA with Tukey test for multiple comparisons in (B, D, and E).
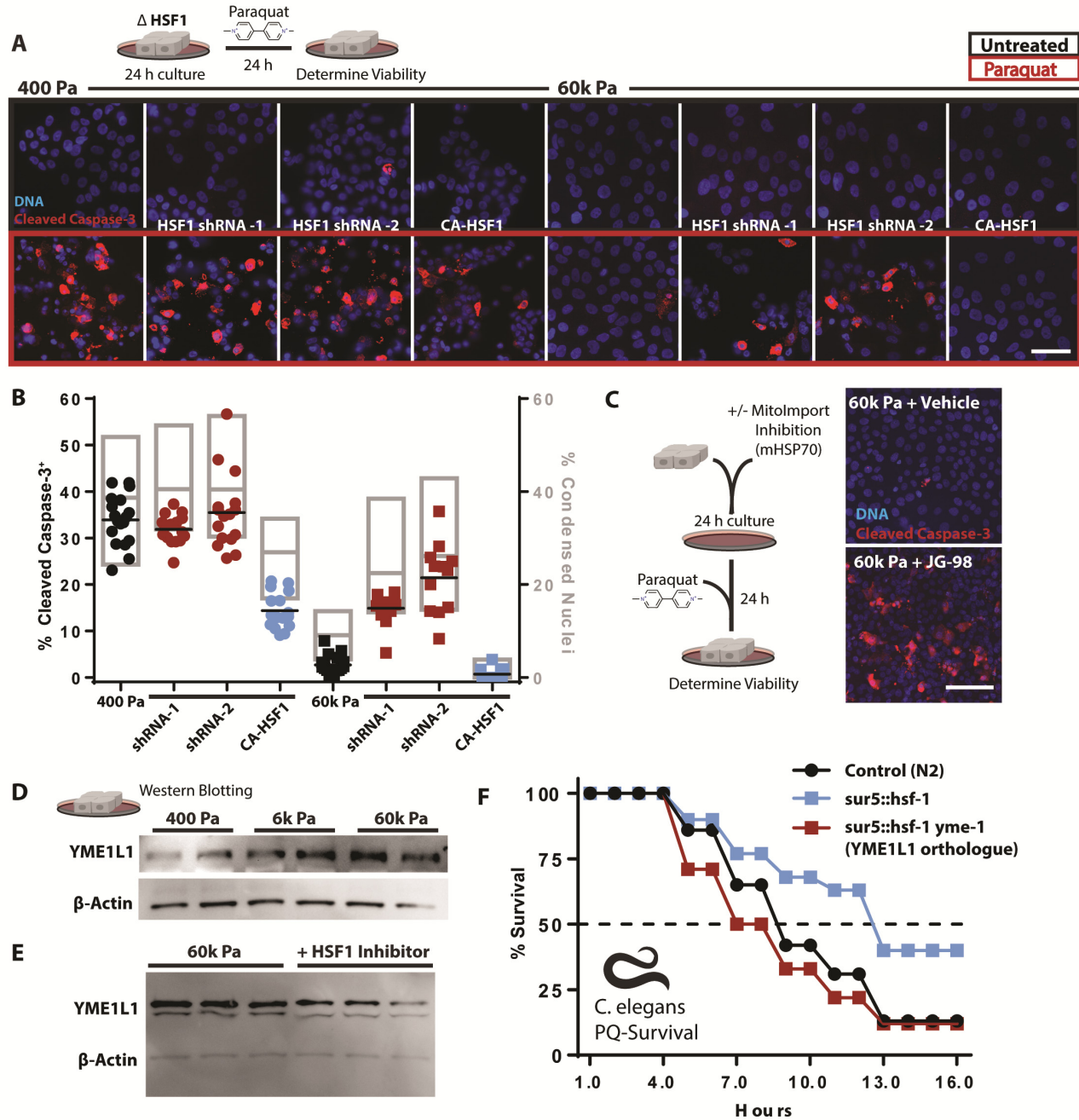
Figure 6: Cytoskeletal tension promotes OxSR *via* HSF1 and YME1L1.

A. Representative microscopy of indicators of apoptosis with cleaved caspase 3 staining (red) and nuclear condensation (dapi) of cells cultured on 400 or 60k Pa PA-gel surfaces for 24 h with subsequent 24 h +/- paraquat treatment [10 mM]. 100k cells/well of 24 well plate. (n=4 replicates, repeated 3 separate times)

B. Quantitation of cells from 16 field views depicted in G for condensed nuclei and cleaved caspase-3 positive cells (1653-575 cells counted per condition, repeated three times).

C. Representative microscopy of indicators of apoptosis with cleaved caspase 3 staining (red) and nuclear condensation (dapi) of cells cultured 60k Pa PA-gel surfaces for 48 h +/- JG98 [1 µM] + 24 h paraquat treatment [10 mM]. 100k cells/well of 24 well plate, repeated twice.

D. Western blot of YME1L1 and β-actin from 5 µg of protein derived from cells cultured on PA-gels for 24 h. (2 biological replicates shown, repeated 3 times)

E. Western blot of YME1L1 and β-actin from 5 µg of protein derived from cells cultured on PA-gels for 24 h +/- KRIBB11 [2 µM] (3 biological replicates shown, repeated 2 times)

F. *C. elegans* survival in 50 mM paraquat, with *C. elegans* overexpressing *hsf-1* (*sur-5p::hsf-1*) compared or control line (N2) grown on either empty vector or *ymel-1* RNAi from hatch (n=80 animals per condition, repeated three times).

Data shown represents ± SEM. *P < 0.05, **P < 0.01, ***P < 0.005, < 0.0001 *via* one-way ANOVA with Tukey test for multiple comparisons in (B and F).

Materials and Methods

Cell culture

MCF10A and MB-MDA-231 cells were sourced from ATCC, routinely tested and found to be free of mycoplasma contamination, and maintained below passage 22. All cells were maintained and in 5% CO^2 at 37 ºC. MCF10A were cultured in [5 mM] glucose DMEM:F12 (1:1 mixture of F:12 [10mM] glucose and [0 mM] glucose DMEM) (Life Technologies, 11765054 and 11966025) supplemented with 5% Horse Serum (Gibco, 16050-122), 20 ng/mL epidermal growth factor (Peprotech), 10 µg/mL insulin (Sigma), 0.5 µg/mL hydrocortisone (Sigma), 100 ng/mL cholera toxin (Sigma, C8052-2MG), and 1x penicillin/streptomycin (Gibco). MB-MDA-231 tumor cells (ATCC) were grown in 5 mM glucose DMEM supplemented with 10% fetal bovine serum (FBS) (Hyclone) and 1x penicillin/streptomycin. HEK293T cells (ATCC) were maintained in DMEM supplemented with 10% FBS and 1x penicillin/streptomycin and were used to produce lentiviral particles with psPAX2 (Addgene 12260), pMD2.G (Addgene 12259) and various transfer vectors described hereafter (https://www.addgene.org/guides/lentivirus/).

Polyacrylamide hydrogel cell culture surfaces (PA-gels)

Cleaned (10% ClO, 1M HCL, then 100% EtOH) round #1 German glass coverslips (Electron Microscopy Services) were coated with 0.5% v/v (3-Aminopropyl)triethoxysilane (APTES, Sigma, 440140), 99.2% v/v ethanol, and 0.3% v/v glacial acetic acid for 2 h and then cleaned in 100% EtOH on an orbital shaker at 22 ºC. APTES activated coverslips were coated with PBS buffered acrylamide / bis-acrylamide (Bio-Rad, 1610140 and 1610142) solutions (3% / 0.05% for 400 Pa, 7.5% / 0.07% for 6k Pa, and 10% /   polymerized with TEMED (0.1% v/v) (Bio-Rad, 1610801) and Potassium Persulfate (0.1% w/v) (Fisher, BP180) to yield a final thickness of ~ 85 µm. PA-gels were washed with 70% EtOH and sterile PBS prior 3,4-dihydroxy-L-phenylalanine (DOPA) coating for 5 min at 22 ºC protected from light with sterile filtered DOPA in pH 10 [10 mM] Tris buffer (*1*). DOPA coated PA-gels were washed 2x with sterile PBS and ECM functionalized with 5 µg/mL human fibronectin (Millipore, FC010) in sterile PBS 1h at 37 ºC to generate an expected fibronectin coating density of 6 µM/cm^2.

Immunofluorescence microscopy

Cells or tissues were fixed in 4% paraformaldehyde (Electron Microscopy Services, 15710) in 1X PBS for 30 min at room temperature, washed and blocked with a blocking buffer (HBSS fortified with: 10% FBS (Hyclone), 0.1% BSA (Fischer, BP1600), 0.05% saponin (EMD, L3771), and 0.1% Tween 20 (Fischer, BP337500). Primary antibodies [1:100-1:200] for 2 h at RT or 24 h at 4 ºC, Secondary antibodies [1:1000] for 2 h at 22 ºC. Samples were imaged with a Nikon Eclipse Ti spinning disc microscope, Yokogawa CSU-X, Andor Zyla sCMOS, Andor Multi-Port Laser unit, and Molecular Devices MetaMorph imaging suite.

Antibodies used: Cleaved Caspase-3 (Asp175) (Cell Signaling, 9661), HSF1 (Cell Signaling, HSF1 4356), and HSP60 (LK1, sc-59567).

MitoTacker staining

Mitotracker deep red FM or Mitotracker Green FM (Invitrogen, M22426 and M7514) was solubilized in DMSO to yield 100 µM frozen aliquots which were diluted into media to yield a 10 µM stock which was added directly to cell culture media already in the culture yielding a final

1

concertation of 100 nM (to prevent media change derived fluid flow shear stress) 30 min before 4% PFA fixation or live cell imaging (MitoTracker red FM was used for PFA fixed samples).

TMRE, H2DCFDA, Rhod-2 AM, Calcium Green-1 AM, and MitoPy1

Stained cells were washed twice with PBS and imaged on a SpectraMax i5 Multi-Mode plate reader. Experiments were carried out in with 50k or 100k cells per well in 500 µL of media in 24 well format with or without fibronectin coated PA-gels (indicated). 2 µM Rhod-2 AM (Thermo, R1244) and 2 µM Calcium green-1 AM (Life Technologies, C3011MP) was added to culture media and allowed to stain at 22 ºC for 20 min prior to imaging (frozen Rhod-2 AM aliquots were used only when the DMSO suspension remained clear), or 2 µM H_2DCFDA (Thermo, D399) was added to media 1 or 4 h prior to imaging, or 5 µM MitoPy1 (Tocris, 4428) was added to media 1 h prior to imaging, 2 nM TMRE (Fischer, T669) was applied to cells in media without disturbing the existing culture media (similar dilution scheme to MitoTracker) for 1 h prior to microscopy or plate reader assay.

Intracellular pH (pH_i)

10 µM BECEF (Invitrogen, B1150) was added to cell culture media for 30 min at 37 °C in 5 % CO_2 incubator. Cultures were washed twice and then fluorescent intensities of BCECF was determined with a SpectraMax i5 plate reader in a buffer comprised of 25 mM HEPES, 140 mM NaCl, 5 mM KCl, 1 mM $KHPO_4$, 1 mM $MgSO_4$, 2 mM $CaCl_2$, and 5 or 25 mM glucose. The cultures were then treated with a pH 7.7 buffer containing 10 µM Nigericin (Invitrogen, N1495), 25 mM HEPES, 105 mM KCl, and 1 mM MgCl for 5 min at 22 °C followed by determination of BCECF fluorescent intensities at high pH. The cultures were then treated with a pH 6.6 buffer containing 10 µM Nigericin (Invitrogen, N1495), 25 mM HEPES, 105 mM KCl, and 1 mM MgCl for 5 min at 22 °C followed by determination of BCECF fluorescent intensities at low pH. A linear relationship between pH 6.6 and 7.7 was observed and sample pH was estimated relative to pH standards for each individual culture well.

qPCR

Total RNA was isolated from biological samples with TRIzol (Invitrogen, 15596-018) according to the manufacturer's instructions. cDNA was synthesized with 1 µg total RNA in 10 µL reaction volume with RNA using M-MLV reverse transcriptase (BioChain, Z5040002-100K) and 5X reaction buffer (BioChain, Z5040002-100K), random hexamers (Roche, 11034731001), dNTPs , and 1U of Ribolock (ThermoFischer, EO0384). RT-thermocycler program: random hexamers and RNA incubated at 70ºC for 10 min, then held at 4ºC until the addition of the M-MLV reverse transcriptase, dNTPs, Ribolock, and M-MLV-reverse transcriptase, then 50ºC for 1 h, 95 ºC for 5 min, then stored at -20 ºC until qPCR was performed. The reverse transcription reaction was then diluted to 50 µL total volume with ddH_2O rendering a concentration of 20 ng RNA per 1 µL used in subsequent qPCR reactions. qPCR was performed in triplicate using PerfeCTa SYBR Green FastMix (Quantabio, Cat# 95072-05K) with an Eppendorf Mastercycler RealPlex^2. qPCR thermocycler program: 95° C for 10 min, then 40 cycles of a 95°C for 15 s, 60°C for 20 s, followed by a melt curve 60-95°C over 10 min. Melt curves and gel electrophoresis were used to validate the quality of amplified products. The ΔCt values from independent experiments were used to calculate fold change of expression using the $2^{-\Delta\Delta Ct}$ method. For each gene measured, the SEM of the ΔCt values was calculated and used to generate positive and negative error values in the $2^{-\Delta\Delta Ct}$ fold change space. Plots of qPCR data display bars representing the mean

fold change ±SEM and individual points representing the fold change value for each experiment relative to the mean.

qPCR primers used:

	5'-Forward	5'-Reverse
UCP2	GGTGGTCGGAGATACCAAAG	CTCGGGCAATGGTCTTGTAG
NRF2	CGGTATGCAACAGGACATTG	ACTGGTTGGGGTCTTCTGTG
18S	GGACACGGACAGGATTGACA	ACCCACGGAATCGAGAAAGA
PKM1	CTATCCTCTGGAGGCTGTGC	CCATGAGGTCTGTGGAGTGA
PKM2	CCACTTGCAATTATTTGAGGAA	GTGAGCAGACCTGCCAGACT
TFAM	AAGATTCCAAGAAGCTAAGGGTGA	CAGAGTCAGACAGATTTTTCCAGTTT
HNRNPA1	CCTTTGACGACCATGACTCC	ACGACCGAAGTTGTCATTCC
ATF5	CTGGCTCCCTATGAGGTCCTTG	GAGCTGTGAAATCAACTCGCTCAG
HSPD1	GATGCTGTGGCCGTTACAATG	GTCAATTGACTTTGCAACAGTCACAC
HSPA9	CAAGCGACAGGCTGTCACCAAC	CAACCCAGGCATCACCATTGG
HSPE1	TGGCAGGACAAGCGTTTAG	GGTTACAGTTTCAGCAGCAC
LONP1	CATTGCCTTGAACCCTCTC	ATGTCGCTCAGGTAGATGG
HSF1	GCCTTCCTGACCAAGCTGT	AAGTACTTGGGCAGCACCTC
XBP1sp	TGCTGAGTCCGCAGCAGGTG	GCTGGCAGGCTCTGGGGAAG
CHOP	GCACCTCCCAGAGCCCTCACTCTCC	GTCTACTCCAAGCCTTCCCCCTGCG
GAPDH	CGACCACTTTGTCAAGCTCA	AGGGGAGATTCA GTGTGGTG
LOX	GAACCAGGTAGCTGGGGTTT	TATGGCTACCACAGGCGATT

Western blotting

Cells were freeze (-80 ºC) thaw lysed with RIPA buffer (150 mM NaCl, 1% v/v NP-40, 0.5% w/v sodium deoxycholate, 0.1% w/v SDS, and 25 mM tris) containing protease and phosphatase inhibitor coctail (GenDepot, P3100 and P3200). Protein content was determined via BCA (Pierce, 23225) and 5-10 µg of protein was mixed with 5x Laemmli buffer to generate final 1x concentration (50 mM Tris-HCl (Fischer, AAJ2267636) pH 6.8, 4% w/v SDS (Sigma, L3771), 10% v/v glycerol (Fischer, BP229-1), 0.1% w/v bromophenol blue (Bio-Rad, 1610404), 2% v/v β-mercaptoethanol (Bio-Rad, 1610710) and heated to 95 ºC for 5 min (no heating of the samples used for the total oxphos (abcam, ab110413) blots). 10%-gels (Bio-Rad, Bulletin_6201) were cast in a PROTEAN Plus multi casting chamer (Bio-Rad). Samples were loaded (~20 µL) and run to completion in Tris Glycine SDS running buffer (25 mM Tris, 192 mM glycine (Fischer, BP381), and 0.1% SDS, pH ~8.6), wet transferred @ 100V for 60 min to methanol (Fischer, A412) activated PVDF (BioRad, 1620177) in Towbin transfer buffer containing (25 mM Tris, 192 mM Glycine, 20% v/v methanol, pH ~8.3). Protein loaded PVDF membranes were washed 2x with TBST (20 mM tris, 150 mM NaCl (S271), 0.1% w/v Tween20) and blocked in 5% milk TBST buffer for 1h at 22 ºC on an orbital shaker.

Antibodies used: HSF1 (Cell Signaling, HSF1 4356), YME1L1 (Invitrogen, PA564299, HSP60 (LK1, sc-59567), HSP70 (3A3, sc32239), mtHSP70 ((D-9), sc-133137), Total OXPHOS WB Antibody Cocktail (ab110413), β-Actin (Sigma,A5441), FAK pY397 (Invitrogen, 44-625G), FAK (BD, 610088), and pMLCK (Cell Signaling, 3671)

ROCK:ER

3

pBABEpuro3 ROCK:ER (*2*) was generously provided by Dr. Michael F. Olson, packaged into retroviral particles with phoenix cells, and used to generate stable MCF10A cells lines which were activated with 1 μg/mL 4-Hydroxytamoxifen (Sigma).

MTS-roGFP2

COX4L MTS tagged roGFP was expressed under the CMV promoter in a puromycin lentiviral transfer vector generated by the Dillin Lab (Dr. Brant Webster).

ATGCTTGCCACTAGAGTCTTTTCATTGGTAGGTAAAAGGGCCATAAGTACATCAGTCTGCG
TGAGAGCCCACACCGGACCGGTCAGCAAGGGCGAGGAGCTGTTCACCGGGGTGGTGCCC
ATCCTGGTCGAGCTGGACGGCGACGTAAACGGCCACAAGTTCAGCGTGTCCGGCGAGGG
CGAGGGCGATGCCACCTACGGCAAGCTGACCCTGAAGTTCATCAGCACCACCGGCAAGCT
GCCCGTGCCCTGGCCCACCCTCGTGACCACCCTGACCTACGGCGTGCAGTGCTTCAGCC
GCTACCCCGACCACATGAAGCGGCACGACTTCTTCAAGTCCGCCATGCCCGAAGGCTACG
TCCAGGAGCGCACCATCTTCTTCAAGGACGACGGCAACTACAAGACCCGCGCCGAGGTGA
AGTTCGAGGGCGACACCCTGGTGAACCGCATCGAGCTGAAGGGCATCGACTTCAAGGAG
GACGGCAACATCCTGGGGCACAAGCTGGAGTACAACTACAACTGCCACAACGTCTATATC
ATGGCCGACAAGCAGAAGAACGGCATCAAGGTGAACTTCAAGATCCGCCACAACATCGAG
GACGGCAGCGTGCAGCTCGCCGACCACTACCAGCAGAACACCCCCATCGGCGACGGCCC
CGTGCTGCTGCCCGACAACCACTACCTGAGCACCTGCTCCGCCCTGAGCAAAGACCCCAA
CGAGAAGCGCGATCACATGGTCCTGCTGGAGTTCGTGACCGCCGCCGGGATCACTCTCG
GCATGGACGAGCTGTACAAGTAA

V737N β1 integrin

Weaver lab generated (Dr. Jonathan Lakins) puromycin lentiviral transfer vector expressing 3x myc tagged V737N β1 integrin using the tetracycline rtTA2(S)-M2 (*3*) inducible promoter for 24 h with doxycycline [200 ng/mL] (Sigma, D9891). No respiratory repression of MCF10A or MB-MDA-231 cells was observed with 200 ng/mL, 1 μg/mL, or 2 μg/mL doxycycline. Previous studies have demonstrated that 24 h of 30 μg/mL doxycycline treatment can suppress mitochondrial respiration (*4*).

ATGAATTTACAACCAATTTTCTGGATTGGACTGATCAGTTCAGTTTGCTGTGTGTTTGCTCA
AACAGATGGCGAGCAGAAGCTGATCAGCGAGGAGGACCTGGGCGAGCAGAAGCTGATCA
GCGAGGAGGACCTGGGCGAGCAGAAGCTGATCAGCGAGGAGGACCTGGGCGGCGCCCA
AACAGATGAAAATCGATGTTTAAAAGCAAATGCCAAATCATGTGGAGAATGTATACAAGCAG
GGCCAAATTGTGGGTGGTGCACAAATTCAACATTTTTACAGGAAGGAATGCCTACTTCTGC
ACGATGTGATGATTTAGAAGCCTTAAAAAAGAAGGGTTGCCCTCCAGATGACATAGAAAAT
CCCAGAGGCTCCAAAGATATAAAGAAAAATAAAAATGTAACCAACCGTAGCAAAGGAACAG
CAGAGAAGCTCAAGCCAGAGGATATTACTCAGATCCAACCACAGCAGTTGGTTTTGCGATT
AAGATCAGGGGAGCCACAGACATTTACATTAAAATTCAAGAGAGCTGAAGACTATCCCATT
GACCTCTACTACCTTATGGACCTGTCTTACTCAATGAAAGACGATTTGGAGAATGTAAAAAG
TCTTGGAACAGATCTGATGAATGAAATGAGGAGGATTACTTCGGACTTCAGAATTGGATTT
GGCTCATTTGTGGAAAAGACTGTGATGCCTTACATTAGCACAACACCAGCTAAGCTCAGGA
ACCCTTGCACAAGTGAACAGAACTGCACCAGCCCATTTAGCTACAAAAATGTGCTCAGTCT
TACTAATAAAGGAGAAGTATTTAATGAACTTGTTGGAAAACAGCGCATATCTGGAAATTTGG
ATTCTCCAGAAGGTGGTTTCGATGCCATCATGCAAGTTGCAGTTTGTGGATCACTGATTGG
CTGGAGGAATGTTACACGGCTGCTGGTGTTTTCCACAGATGCCGGGTTTCACTTTGCTGGA

GATGGGAAACTTGGTGGCATTGTTTTACCAAATGATGGACAATGTCACCTGGAAAATAATAT
GTACACAATGAGCCATTATTATGATTATCCTTCTATTGCTCACCTTGTCCAGAAACTGAGTG
AAAATAATATTCAGACAATTTTTGCAGTTACTGAAGAATTTCAGCCTGTTTACAAGGAGCTG
AAAAACTTGATCCCTAAGTCAGCAGTAGGAACATTATCTGCAAATTCTAGCAATGTAATTCA
GTTGATCATTGATGCATACAATTCCCTTTCCTCAGAAGTCATTTTGGAAAACGGCAAATTGT
CAGAAGGAGTAACAATAAGTTACAAATCTTACTGCAAGAACGGGGTGAATGGAACAGGGG
AAAATGGAAGAAAATGTTCCAATATTTCCATTGGAGATGAGGTTCAATTTGAAATTAGCATA
ACTTCAAATAAGTGTCCAAAAAAGGATTCTGACAGCTTTAAAATTAGGCCTCTGGGCTTTAC
GGAGGAAGTAGAGGTTATTCTTCAGTACATCTGTGAATGTGAATGCCAAAGCGAAGGCATC
CCTGAAAGTCCCAAGTGTCATGAAGGAAATGGGACATTTGAGTGTGGCGCGTGCAGGTGC
AATGAAGGGCGTGTTGGTAGACATTGTGAATGCAGCACAGATGAAGTTAACAGTGAAGACA
TGGATGCTTACTGCAGGAAAGAAAACAGTTCAGAAATCTGCAGTAACAATGGAGAGTGCGT
CTGCGGACAGTGTGTTTGTAGGAAGAGGGATAATACAAATGAAATTTATTCTGGCAAATTCT
GCGAGTGTGATAATTTCAACTGTGATAGATCCAATGGCTTAATTTGTGGAGGAAATGGTGTT
TGCAAGTGTCGTGTGTGTGAGTGCAACCCCAACTACACTGGCAGTGCATGTGACTGTTCTT
TGGATACTAGTACTTGTGAAGCCAGCAACGGACAGATCTGCAATGGCCGGGGCATCTGCG
AGTGTGGTGTCTGTAAGTGTACAGATCCGAAGTTTCAAGGGCAAACGTGTGAGATGTGTCA
GACCTGCCTTGGTGTCTGTGCTGAGCATAAAGAATGTGTTCAGTGCAGAGCCTTCAATAAA
GGAGAAAAGAAAGACACATGCACACAGGAATGTTCCTATTTTAACATTACCAAGGTAGAAA
GTCGGGACAAATTACCCCAGCCGGTCCAACCTGATCCTGTGTCCCATTGTAAGGAGAAGG
ATGTTGACGACTGTTGGTTCTATTTTACGTATTCAGTGAATGGGAACAACGAGGTCATGGTT
CATGTTGTGGAGAATCCAGAGTGTCCCACTGGTCCAGACATCATTCCAATTGTAGCTGGTG
TT**AAC**GCTGGAATTGTTCTTATTGGCCTTGCATTACTGCTGATATGGAAGCTTTTAATGATA
ATTCATGACAGAAGGGAGTTTGCTAAATTTGAAAAGGAGAAAATGAATGCCAAATGGGACA
CGGGTGAAAATCCTATTTATAAGAGTGCCGTAACAACTGTGGTCAATCCGAAGTATGAGGG
AAAATGA

WT β1 integrin

Weaver lab generated (Dr. Jonathan Lakins) puromycin lentiviral transfer vector expressing 3x myc tagged β1 integrin using the tetracycline rtTA2(S)-M2 (*3*) inducible promoter for 24 h with doxycycline [200 ng/mL] (Sigma, D9891).

ATGAATTTACAACCAATTTTCTGGATTGGACTGATCAGTTCAGTTTGCTGTGTGTTTGCTCA
AACAGATGGCGAGCAGAAGCTGATCAGCGAGGAGGACCTGGGCGAGCAGAAGCTGATCA
GCGAGGAGGACCTGGGCGAGCAGAAGCTGATCAGCGAGGAGGACCTGGGCGGCGCCCA
AACAGATGAAAATCGATGTTTAAAAGCAAATGCCAAATCATGTGGAGAATGTATACAAGCAG
GGCCAAATTGTGGGTGGTGCACAAATTCAACATTTTTACAGGAAGGAATGCCTACTTCTGC
ACGATGTGATGATTTAGAAGCCTTAAAAAAGAAGGGTTGCCCTCCAGATGACATAGAAAAT
CCCAGAGGCTCCAAAGATATAAAGAAAAATAAAAATGTAACCAACCGTAGCAAAGGAACAG
CAGAGAAGCTCAAGCCAGAGGATATTACTCAGATCCAACCACAGCAGTTGGTTTTGCGATT
AAGATCAGGGGAGCCACAGACATTTACATTAAAATTCAAGAGAGCTGAAGACTATCCCATT
GACCTCTACTACCTTATGGACCTGTCTTACTCAATGAAAGACGATTTGGAGAATGTAAAAAG
TCTTGGAACAGATCTGATGAATGAAATGAGGAGGATTACTTCGGACTTCAGAATTGGATTT
GGCTCATTTGTGGAAAAGACTGTGATGCCTTACATTAGCACAACACCAGCTAAGCTCAGGA
ACCCTTGCACAAGTGAACAGAACTGCACCAGCCCATTTAGCTACAAAAATGTGCTCAGTCT
TACTAATAAAGGAGAAGTATTTAATGAACTTGTTGGAAAACAGCGCATATCTGGAAATTTGG
ATTCTCCAGAAGGTGGTTTCGATGCCATCATGCAAGTTGCAGTTTGTGGATCACTGATTGG

CTGGAGGAATGTTACACGGCTGCTGGTGTTTTCCACAGATGCCGGGTTTCACTTTGCTGGA
GATGGGAAACTTGGTGGCATTGTTTTACCAAATGATGGACAATGTCACCTGGAAAATAATAT
GTACACAATGAGCCATTATTATGATTATCCTTCTATTGCTCACCTTGTCCAGAAACTGAGTG
AAAATAATATTCAGACAATTTTTGCAGTTACTGAAGAATTTCAGCCTGTTTACAAGGAGCTG
AAAAACTTGATCCCTAAGTCAGCAGTAGGAACATTATCTGCAAATTCTAGCAATGTAATTCA
GTTGATCATTGATGCATACAATTCCCTTTCCTCAGAAGTCATTTTGGAAAACGGCAAATTGT
CAGAAGGAGTAACAATAAGTTACAAATCTTACTGCAAGAACGGGGTGAATGGAACAGGGG
AAAATGGAAGAAATGTTCCAATATTTCCATTGGAGATGAGGTTCAATTTGAAATTAGCATA
ACTTCAAATAAGTGTCCAAAAAAGGATTCTGACAGCTTTAAAATTAGGCCTCTGGGCTTTAC
GGAGGAAGTAGAGGTTATTCTTCAGTACATCTGTGAATGTGAATGCCAAAGCGAAGGCATC
CCTGAAAGTCCCAAGTGTCATGAAGGAAATGGGACATTTGAGTGTGGCGCGTGCAGGTGC
AATGAAGGGCGTGTTGGTAGACATTGTGAATGCAGCACAGATGAAGTTAACAGTGAAGACA
TGGATGCTTACTGCAGGAAAGAAACAGTTCAGAAATCTGCAGTAACAATGGAGAGTGCGT
CTGCGGACAGTGTGTTTGTAGGAAGAGGGATAATACAAATGAAATTTATTCTGGCAAATTCT
GCGAGTGTGATAATTTCAACTGTGATAGATCCAATGGCTTAATTTGTGGAGGAAATGGTGTT
TGCAAGTGTCGTGTGTGTGAGTGCAACCCCAACTACACTGGCAGTGCATGTGACTGTTCTT
TGGATACTAGTACTTGTGAAGCCAGCAACGGACAGATCTGCAATGGCCGGGGCATCTGCG
AGTGTGGTGTCTGTAAGTGTACAGATCCGAAGTTTCAAGGGCAAACGTGTGAGATGTGTCA
GACCTGCCTTGGTGTCTGTGCTGAGCATAAAGAATGTGTTCAGTGCAGAGCCTTCAATAAA
GGAGAAAAGAAAGACACATGCACACAGGAATGTTCCTATTTTAACATTACCAAGGTAGAAA
GTCGGGACAAATTACCCCAGCCGGTCCAACCTGATCCTGTGTCCCATTGTAAGGAGAAGG
ATGTTGACGACTGTTGGTTCTATTTTACGTATTCAGTGAATGGGAACAACGAGGTCATGGTT
CATGTTGTGGAGAATCCAGAGTGTCCCACTGGTCCAGACATCATTCCAATTGTAGCTGGTG
TGGTTGCTGGAATTGTTCTTATTGGCCTTGCATTACTGCTGATATGGAAGCTTTTAATGATA
ATTCATGACAGAAGGGAGTTTGCTAAATTTGAAAAGGAGAAATGAATGCCAAATGGGACA
CGGGTGAAAATCCTATTTATAAGAGTGCCGTAACAACTGTGGTCAATCCGAAGTATGAGGG
AAAATGA

In vitro respirometry

Mitochondrial stress tests were performed with a Seahorse XF24e cellular respirometer on non-permeablized cells at ~ 96% confluence (100k cells/well) in V7 microplates, with XF assay medium supplemented with 1 mM pyruvate (Gibco), 2 mM glutamine (Gibco),and 5 or 25 mM glucose (Sigma) at pH 7.4 and sequential additions via injection ports of Oligomycin [1 mM final], FCCP [1 mM final], and Antimycin A/Rotenone [1 mM final] during respirometry (concentrated stock solutions solubilized in 100% ethanol [2.5 mM] for mitochondrial stress test compounds). OCR values presented with non-mitochondrial oxygen consumption deducted.

Atomic force microscopy

AFM and analyses were performed using an MFP3D-BIO inverted optical atomic force microscope mounted on a Nikon TE2000-U inverted fluorescence microscope (Asylum Research). 100k cells were seeded onto fibronectin coated 15 mm^2 coverslips and cultured for 24 h. Coverslips were anchored with permanent adhesive dots (Scotch, 00051141908113) to a glass slide that was then magnet-anchored to the stage of the microscope. All samples were measured in media with contact mode using Novascan cantilevers (5 μm radius, Probe 58, k = 0.06 N per m), which were calibrated using the thermal tune method. 36 force measurements were collected over a 250 × 250 μm grid per sample. The resulting force data were converted to elastic modulus values using the Hertz Model program (tissue samples were assumed to be

6

noncompressible, and a Poisson's ratio of 0.5 was used in the calculation of theYoung's elastic modulus values) in IgorPro v.6.22, supplied by Asylum Research

Knockdown of HSF1

pLKO.1 puro (Addgene #8453) was modified to carry:
Scr insert:
5'-CAACAAGATGAAGAGCACCAACTCGAGTTGGTGCTCTTCATCTTGTTGTTTTT,
shRNA HSF1-1 TRCN0000007481 (HSF1):
5'-CCGGGCAGGTTGTTCATAGTCAGAACTCGAGTTCTGACTATGAACAACCTGCTTTTT,
shRNA HSF1-2 TRCN0000318652 (HSF1):
5'-CCGGGCACATTCCATGCCCAAGTATCTCGAGATACTTGGGCATGGAATGTGCTTTTT

Constitutively active HSF1

CD510B-1_pCDH-CMV-MCS-EF1-Puro (SystemBio) vector was modified to carry the hHSF1ΔRD (Δ221–315) transgene (*5*) under the CMV promoter.

ATGGATCTGCCCGTGGGCCCCGGCGCGGCGGGGCCCAGCAACGTCCCGGCCTTCCTGA
CCAAGCTGTGGACCCTCGTGAGCGACCCGGACACCGACGCGCTCATCTGCTGGAGCCCG
AGCGGGAACAGCTTCCACGTGTTCGACCAGGGCCAGTTTGCCAAGGAGGTGCTGCCCAA
GTACTTCAAGCACAACAACATGGCCAGCTTCGTGCGGCAGCTCAACATGTATGGCTTCCG
GAAAGTGGTCCACATCGAGCAGGGCGGCCTGGTCAAGCCAGAGAGAGACGACACGGAGT
TCCAGCACCCATGCTTCCTGCGTGGCCAGGAGCAGCTCCTTGAGAACATCAAGAGGAAAG
TGACCAGTGTGTCCACCCTGAAGAGTGAAGACATAAAGATCCGCCAGGACAGCGTCACCA
AGCTGCTGACGGACGTGCAGCTGATGAAGGGGAAGCAGGAGTGCATGGACTCCAAGCTC
CTGGCCATGAAGCATGAGAATGAGGCTCTGTGGCGGGAGGTGGCCAGCCTTCGGCAGAA
GCATGCCCAGCAACAGAAAGTCGTCAACAAGCTCATTCAGTTCCTGATCTCACTGGTGCAG
TCAAACCGGATCCTGGGGGGTGAAGAGAAAGATCCCCCTGATGCTGAACGACAGTGGCTCA
GCACATGGGCGCCCATCTTCCGTGGACACCCTCTTGTCCCCGACCGCCCTCATTGACTCC
ATCCTGCGGGAGAGTGAACCTGCCCCCGCCTCCGTCACAGCCCTCACGGACGCCAGGGG
CCACACGGACACCGAGGGCCGGCCTCCCTCCCCCCCGCCCACCTCCACCCCTGAAAAGT
GCCTCAGCGTAGCCTGCCTGGACAAGAATGAGCTCAGTGACCACTTGGATGCTATGGACT
CCAACGAGGATAACCTGCAGACCATGCTGAGCAGCCACGGCTTCAGCGTGGACACCAGTG
CCCTGCTGGACCTGTTCAGCCCCTCGGTGACCGTGCCCGACATGAGCCTGCCTGACCTTG
ACAGCAGCCTGGCCAGTATCCAAGAGCTCCTGTCTCCCCAGGAGCCCCCCAGGCCTCCC
GAGGCAGAGAACAGCAGCCCGGATTCAGGGAAGCAGCTGGTGCACTACACAGCGCAGCC
GCTGTTCCTGCTGGACCCCGGCTCCGTGGACACCGGGAGCAACGACCTGCCGGTGCTGT
TTGAGCTGGGAGAGGGCTCCTACTTCTCCGAAGGGGACGGCTTCGCCGAGGACCCCACC
ATCTCCCTGCTGACAGGCTCGGAGCCTCCCAAAGCCAAGGACCCCACTGTCTCCTAG

SLC9A1 KO

MCF10A cells were transfected v*ia* PEI (https://www.addgene.org/protocols/transfection/) with pSpCas9(BB)-2A-GFP (PX458) - (Addgene #48138) carrying sgRNA for hSLC9A1 KO 5'-GTTTGCCAACTACGAACACG (SLC9A1:HGLibA_45399) and H^+-suicide selected (*6*) four separate times to isolate SCL9A1 KOs. ~15% of the cells survived the first H^+-suicide selection, ~90% survived the subsequent 4 sections.

C. elegans strains and maintenance

All *C. elegans* strains are derivatives of the Bristol N2 strain from Caenorhabditis Genetics Center (CGC) and are listed below. All worms are maintained at 15 °C on standard nematode growth media (NGM) plates and fed OP50 *E. coli* B bacteria and are maintained for a maximum of 20-25 generations (weeks). For all experiments, worms are synchronized using a standard bleaching protocol by degrading carcasses with bleach solution (1.8% sodium hypochlorite, 0.375M KOH), then washing eggs four times with M9 solution (22 mM KH_2PO_4 monobasic, 42.3 mM Na_2HPO_4, 85.6 mM NaCl, 1 mM $MgSO_4$), followed by L1 arresting synchronization, achieved by floating eggs in M9 overnight in a 20 °C incubator on a rotator for a maximum of 16 hours. L1s are plated on RNAi bacteria (NGM + 1 µM IPTG and 100 µg/mL carbenicillin; HT115 *E. coli* K strain containing pL4440 vector control or pL4440 with RNAi of interest) until the desired stages of adulthood. All RNAi constructs were isolated from the Vidal library and verified sequences are available below.

C. elegans strains		
C. elegans: Bristol (N2) strain as wild type (WT)	CGC	-
C. elegans: AGD710: N2, uthIs235[sur-5p::hsf-1, myo-2p::tdTomato]	Dillin Lab	(7)
C. elegans: AGD2319: N2; unc-119(ed3) III; uthSi62[vha-6p::MLS::mRuby::unc-54 3'UTR, cb-unc-119(+)] IV;	Dillin Lab	This study
C. elegans: AGD2490: N2; uthIs235[sur-5p::hsf-1, myo-2p::tdTomato]; dvIs19[pAF15(gst-4p::GFP::NLS)]	Dillin Lab	This study
C. elegans: CL2166: N2; gst-4p::GFP	CGC	(7)

hsf-1

CGTCAGCGCGCCCGTACCGGCACATCAAATCCATTTTCCGGGTACTGTTGCTCATTATCAA
ACAACAAATCCTCGGCTCCATCATAATTCGACGTCTCCGGAGCATTTTCAAGAGCAAGCTG
TCTGAGTGGATCCTCGGATCCTTCTTCATCATCATCCAACGGTACATTATTCCCAAAATCAT
CCCAATTATGATTACTGACTAAATCTCTGAAACTCTCCAATGAAGTATCAGTTCCAGTGAAA
TATTCTTGAAGTTCTTGAGATAATTGACGATCAAATGATGGAGAGAGTCCGAGAGTTGGAG
AATATAGATTTTGATGAGGATCTGCGTTGGTGGATGAGGTGGAAGTCGTTGGATGATGCTG
ATCTTCTATTGCCATTAGCTTCTGATGCGGTTGAAGGTATTGATGAGATGGTTGATATGGAA
TCATTGAAGGATCTGAAGGCATGAAGCCACTGTAATTGTTCACAAATCCTCCCGAATAGTCT
TGTTGCGGCTGAAAATTTCGAATTTTTAGAC

nhx-2

GTCAACGAAGTTCTTTTTATTGCCGTGTTCGGAGAATCTCTATTGAACGACGGAGTTGCTGT
TGTACTTTATCGAATGTTCTTGACCTTCTCTGAAATTGGAACTGAGAATCTGATAACATCTG
ATTATATCAATGGAGGTGTTTCTTTCCTGGTTGTTGCATTTGGTGGAATTGGAATTGGTCTT
CTTTTTGCATTTTTGACAAGTCTTGTTACAAGATTTGCTAGAGATGAAGAGGTCAAAGTGCT
CAATTCTGTATTTATTCTCATTCTTCCGTACACTTGTTATCTTTGTGGAGAACTTTTCGGTCT
TTCAAGTATTATGGC

skn-1

*TGTACACGGACAGCAATAATAGGAGCTTTGATGAAGTCAACCATCAGCATCAACAAGAACA
AGATTTCAATGGCCAATCCAAATATGATTATCCACAATTCAACCGTCCAATGGGTCTCCGTT
GGCGTGATGATCAACGGATGATGGAGTATTTCATGTCGAATGGTCCAGTAGAAACTGTTCC
AGTTATGCCAATACTCACCGAGCATCCACCAGCATCTCCATTCGGTAGAGGACCATCTACA
GAACGTCCAACCACATCATCTCGATACGAGTACAGTTCGCCTTCTCTCGAGGATATCGACT
TGATTGATGTGCTATGGAGAAGTGATATTGCTGGAGAGAAGGGCACACGACAAGTGGCTC
CTGCTGATCAGTACGAATGTGATTTGCAGACGTTGACAGAGAAATCGACAGTAGCG*

ymel-1

*TCGATTCAGTTGGCTCAAAACGTGTTTCGAATTCCATCCATCCATATGCAAATCAAACGATT
AATCAACTTCTCAGGTAACAATTTGCTCAATTTTGTGCATTAAAAACTCATCTCCTGATGTTT
TCAGTGAAATGGATGGCTTCACCCGTAACGAGGGAATCATTGTAATTGCCGCAACAAATCG
TGTCGACGACCTC*

C. elegans compound microscopy of mitochondria

Transgenic animals carrying vha-6p::MLS::mRuby (MLS was derived from *atp-1*: ATGTTGTCCAAACGCATTGTTACCGCTCTTAACACCGCCGTCAAGGTCCAAAATGCCGGAA TCGCCACCACCGCCCGCGGA) were grown from L1 to desired stage of adulthood on standard RNAi plates as described above. Animals were aged by hand-picking adults away from progeny using a pick daily until desired stage of adulthood. For imaging, adult worms are mounted on a glass slide in M9 solution, covered with a cover slip, and imaged immediately for a maximum of 10 minutes per slide. Animals were imaged on a Zeiss AxioObserver.Z1 microscope equipped with a lumencor sola light engine and a Zeiss axiocam 506 camera, driven by Zeiss ZenBlue software using a 63x/1.4 Plan Apochromat objective and a standard dsRed filter was used (Zeiss filter set 43).

C. elegans Paraquat survival assay

Animals were grown to day 1 adulthood on standard RNAi plates as described above. 10 animals were picked into 75 μL of 100 mM paraquat solution prepared in M9 in a flat-bottom 96-well plate. >8 wells are used per condition for a minimum of 80 animals per replicate. Animals were scored every 2 hours for death. Plates are tapped gently, and any trashing or bending movement is scored as alive. Paraquat survival assays are performed with the experimenter blinded to the strain conditions during scoring and are repeated a minimum of 3 replicates per experiment.

C. elegans stereomicroscopy for fluorescent transcriptional reporters

Transgenic animals carrying *gst-4p::GFP* were grown on standard RNAi plates as described above until the L4 stage. L4 animals were washed off of plates using M9, centrifuged to pellet, and M9 was replaced with 50 mM paraquat prepared in M9. Animals were incubated rotating in a 20 °C incubator for two hours, and subsequently washed 2x with M9 solution. Animals were then plated on OP50 plates and recovered for 2 hours at 20 °C. For imaging, worms were picked onto a standard NGM plate containing 5 μL of 100 mM sodium azide to paralyze worms. Paralyzed worms were lined up, and imaged immediately on a Leica M250FA automated fluorescent stereomicroscope equipped with a Hamamatsu ORCA-ER camera, standard GFP filter, and driven by LAS-X software.

C. elegans biosorter analysis

9

For large-scale quantification of fluorescent animals, a Union Biometrica complex object parameter analysis sorter (COPAS) was used (for full details, refer to (*8*)). Briefly, to quantify signal of *gst-4p::GFP*, animals treated as described above were washed off plates using M9, and run through the COPAS biosort using a 488 nm light source. Integrated fluorescence intensity normalized to the time of flight is collected automatically on the COPAS software, and then normalized again to the extinction to correct for both worm length and worm thickness.

For JC-9 staining, day 1 adult animals were transferred to a plate containing JC-9-treated bacteria (OP50 bacteria were grown during mid-log phase for 4 hours in LB containing 50 μM JC-9 at 37 °C to incorporate JC-9 into bacteria; then bacteria were washed 2x with fresh LB to remove excess JC-9). Animals were grown on JC-9 bacteria for 2 hours at 20 °C to label. After labeling, worms were moved onto standard OP50 plates and grown for an additional 1 hour at 20 °C to remove excess JC-9 from the gut. Animals were then washed off plates and immediately run on a biosorter using a 488 and 561 nm light source. Worm profile data was collected, and run through an orientation and quantification algorithm, LAMPro (*8*). Briefly, integrated fluorescence intensity is measured throughout the entire profile of the worm and normalized to extinction throughout the length of the worm. Total integrated fluorescence of the entire worm was also calculated by normalizing to the time of flight and integrated extinction of the entire worm. JC-9 fluorescence at 515 nm was used to determine mitochondrial quantity, and the ratio of the fluorescence of 585 nm / 515 nm was used to determine mitochondrial membrane potential.

Lifespan assay

Lifespan measurements were performed on solid NGM plates with RNAi bacteria. Worms were synchronized via bleaching/L1 arrested as described above. Adult animals were moved away from progeny by moving worms onto fresh RNAi plates every day until D7-10 when progeny were no longer visible. Animals were then scored every 1-2 days for death until all animals were scored. Animals with bagging vulval explosion, or other age-unrelated deaths were censored and removed from quantification.

Lattice Light Sheet Microscopy

We used a Custom build lattice light sheet microscope (*9*) to image MCF10A culture on polyacrylamide gels. Polyacrylamide gels (PA-gels) were formed on 5 mm round cover glass (Warner Instruments), coated with fibronectin and seeded with ~ 1000 cells per gel. The samples were cultured for 24 h in MCF10A media prior to imaging in DMEM (5 mM glucose) without phenol red supplemented with 5% Fetal Bovine serum. Samples were illuminated by 561 nm diode laser (0.5W Coherent) or 639 nm diode laser (1W Coherent) using an excitation objective (Special Optics, 0.65 NA with a working distance of 3.74-mm) at 2% AOTF transmittance and output laser power of 100 mW. The measured powers at the back focal plane of the illumination objective were in the range of 0.15-0.2 mW. Order transfer functions were calculated by acquiring Point-spread functions using 200-nm TetraSpeck beads adhered freshly to 5-mm glass coverslips (Invitrogen T7280) for each excitation wavelength and each acquisition filter set. The LLSM was realigned before each experiment.

For illumination we displayed on the spatial light modulator (SLM) a Square lattice generated by an interference pattern of 59 bessels beams separated by 1.67 um and cropped to 0.22 with a 0.325 inner NA and 0.40 outer NA, or by a an interference pattern of 83 bessels beams

separated by 1.23 um and cropped to 0.22 with a 0.44 inner NA and 0.55 outer NA The lattice light sheet was dithered 15-25 um to obtain an homogenous illumination with 5% of flyback time. Fluorescent signal was collected by a Nikon detection objective (CFI Apo LWD 25XW, 1.1 NA, 2-mm working distance (WD)), coupled with a 500 mm focal length tube lens (Thorlabs), a set of Semrock filters (BL02-561R-25, BLP01-647R-25, and NF03-405-488-561-635E-25), and a sCMOS camera (Hamamatsu Orca Flash 4.0 v2) with a 103 nm/pixel magnification.

Z-Stacks (Volumes) were acquired by moving the Z-piezo in scanning mode while leaving the lattice light sheet static. The slices of the stacks were taken with an interval of 100-235 nm (S-axis) through ranges of 30-35 um at 20-100 ms exposuretime with 0 - 60 seconds intervals between volumes.

Raw data was flash corrected (*10*) and deconvolved using an iterative Richardson-Lucy algorithm (*9*) on two graphics processing units (GPU) (NVIDIA, GeForce GTX TITAN 4 Gb RAM). Flash calibration, flash correction, channel registration, Order transfer function calculation and Image deconvolution were done using the LLSpy open software (*11*). Visualization of the images and volume inspection were done using Spimagine (Github/maweigert/spimagine) and Clear volume (*12*).

For the glucose shock experiment, MCF10A cells were first localized under the LLSM. During the first 30 seconds of the acquisition, the glucose concentration was raised to a final concentration of 25 mM. The glucose infusion caused misalignment of the lattice light sheet microscope which was corrected manually during the first acquisition volume.

RNAseq

Total RNA was isolated using Trizol (Invitrogen), and RNAseq libraries (2 biological replicates per condition comprised of a pool of 4 PA-gel cultures each) prepared using KAPA mRNA HyperPrep Kit (Roche) and IDT dual indexed sequencing adaptors. Multiplexed libraries were sequenced on an Illumina HiSeq4000, and reads were aligned to the human genome (hg19) using RNA STAR (*13*). Aligned reads were counted using HOMER (*14*), and hierarchical clustering was performed using Cluster (*15*) and visualized with Java TreeView. Gene Ontology analysis was performed using Metascape (*16*).

LC-MS/MS Deuterium Incorporation Proteomics

1 million cells were seeded on 50 mM^2 varied stiffness PA-gels cultured for 24h in 6% D_2O culture media in a 5% CO_2 incubator humidified with 5% D_2O. D_2O labeled cells were detached with cold PBS and a cell scraper (rubber policeman), pelleted with centrifugation, and mitochondrial fractions were isolated with the Mitochondria Isolation Kit for Cultured Cells (Thermo, 89874). Protein was isolated by flash freezing and sonication in PBS with 1 mM PMSF, 5 mM EDTA, and 1x Halt protease inhibitor (Thermo, 78440). Protein content was quantified via BCA (Pierce, 23225) and 100 µg of protein from each sample was trypsin (Pierce, 90057) digested overnight after reduction and alkylation with DTT, TFE, and iodoactamide (*17*). Trypsin-digested peptides were analyzed on a 6550 quadropole time of flight (Q-ToF) mass spectrometer equipped with Chip Cube nano ESI source (Agilent Technologies). High performance liquid chromatography (HPLC) separated the peptides using capillary and nano binary flow. Mobile phases were 95% acetonitrile/0.1% formic acid in LC-MS grade water. Peptides were eluted at 350 nL/minute flow rate with an 18 minute LC gradient. Each sample was analyzed once for protein/peptide identification in data-dependent MS/MS mode and once

11

for peptide isotope analysis in MS mode. Acquired MS/MS spectra were extracted and searched using Spectrum Mill Proteomics Workbench software (Agilent Technologies) and a human protein database (www.uniprot.org). Search results were validated with a global false discovery rate of 1%. A filtered list of peptides was collapsed into a nonredundant peptide formula database containing peptide elemental composition, mass, and retention time. This was used to extract mass isotope abundances (M0-M3) of each peptide from MS-only acquisition files with Mass Hunter Qualitative Analysis software (Agilent Technologies). Mass isotopomer distribution analysis (MIDA) was used to calculate peptide elemental composition and curve-fit parameters for predicting peptide isotope enrichment based on precursor body water enrichment (p) and the number (n) of amino acid C-H positions per peptide actively incorporating hydrogen (H) and deuterium (D) from body water. Subsequent data handling was performed using python-based scripts, with input of precursor body water enrichment for each subject, to yield fractional synthesis rate (FSR) data at the protein level. FSR data were filtered to exclude protein measurements with fewer than 2 peptide isotope measurements per protein. Details of FSR calculations and data filtering criteria were described previously (Holmes, W.E., et al., 2015).

LC-MS/MS Metabolomics

1 million cells were seeded on 50 mM^2 varied stiffness PA-gels cultured for 24 h. Cells were dissolved in 100% methanol doped with NEM [8 mM,1 mg/mL] (Sigma-Aldrich, cat. no. E1271) (*18*). Protein concentrations of the methanol extract was determined via BCA (Pierce, 23225) Data was normalized to 100 µg per sample and polar metabolites were extracted in a total volume of 275 µl of 40:40:20 (acetonitrile:methanol:water) with inclusion of internal standard d_3N^{15}-serine (Cambridge Isotope Laboratories, Inc. #DNLM-6863). Extracted samples were centrifuged at 10,000 x g for 10 min and an aliquot of the supernatant was injected onto LC/MS where metabolites were separated by liquid chromatography as previously described (*19*). Analysis was performed with an electrospray ionization (ESI) source on an Agilent 6430 QQQ LC-MS/MS (Agilent Technologies). The capillary voltage was set to 3.0 kV, and the fragmentor voltage was set to 100 V, the drying gas temperature was 350 ºC, the drying gas flow rate was 10 L/min, and the nebulizer pressure was 35 PSI. Polar metabolites were identified by SRM of the transition from precursor to product ions at associated optimized collision energies and retention times as previously described (*20*). Quantification of metabolites was performed by integrating the area under the curve and then normalizing to internal standard values. All metabolite levels are expressed as relative abundances compared to the control group.

Paraquat survival

10 mM paraquat (Acros Organics, 227320010) was dissolved into media and added to cell culture vessels and allowed to affect the cells for 24 h, experiments were always performed with a fresh suspension of paraquat. After 24 h of paraquat treatment cells were fixed with 4% PFA and stained for cleaved caspase 3 (Cell Signaling, 9661).

Supplemental references

1. O. Y. Wouters, D. T. A. Ploeger, S. M. van Putten, R. A. Bank, 3,4-Dihydroxy-L-Phenylalanine as a Novel Covalent Linker of Extracellular Matrix Proteins to Polyacrylamide Hydrogels with a Tunable Stiffness. *Tissue Eng. Part C. Methods*. **22**, 91–101 (2016).

2. D. R. Croft, M. F. Olson, Conditional regulation of a ROCK-estrogen receptor fusion protein. *Methods Enzymol.* **406**, 541–553 (2006).

3. S. Urlinger, U. Baron, M. Thellmann, M. T. Hasan, H. Bujard, W. Hillen, Exploring the sequence space for tetracycline-dependent transcriptional activators: novel mutations yield expanded range and sensitivity. *Proc. Natl. Acad. Sci. U. S. A.* **97**, 7963–7968 (2000).

4. P. M. Quirós, M. A. Prado, N. Zamboni, D. D'Amico, R. W. Williams, D. Finley, S. P. Gygi, J. Auwerx, Multi-omics analysis identifies ATF4 as a key regulator of the mitochondrial stress response in mammals. *J. Cell Biol.* **216**, 2027–2045 (2017).

5. A. Nakai, M. Suzuki, M. Tanabe, Arrest of spermatogenesis in mice expressing an active heat shock transcription factor 1. *EMBO J.* **19**, 1545–1554 (2000).

6. J. Pouysségur, C. Sardet, A. Franchi, G. L'Allemain, S. Paris, A specific mutation abolishing Na+/H+ antiport activity in hamster fibroblasts precludes growth at neutral and acidic pH. *Proc. Natl. Acad. Sci. U. S. A.* **81**, 4833–4837 (1984).

7. N. A. Baird, P. M. Douglas, M. S. Simic, A. R. Grant, J. J. Moresco, S. C. Wolff, J. R. Yates 3rd, G. Manning, A. Dillin, HSF-1-mediated cytoskeletal integrity determines thermotolerance and life span. *Science*. **346**, 360–363 (2014).

8. J. R. Daniele, D. J. Esping, G. Garcia, L. S. Parsons, E. A. Arriaga, A. Dillin, "High-Throughput Characterization of Region-Specific Mitochondrial Function and Morphology." *Sci. Rep.* **7**, 6749 (2017).

9. B.-C. Chen, W. R. Legant, K. Wang, L. Shao, D. E. Milkie, M. W. Davidson, C. Janetopoulos, X. S. Wu, J. A. Hammer 3rd, Z. Liu, B. P. English, Y. Mimori-Kiyosue, D. P. Romero, A. T. Ritter, J. Lippincott-Schwartz, L. Fritz-Laylin, R. D. Mullins, D. M. Mitchell, J. N. Bembenek, A.-C. Reymann, R. Böhme, S. W. Grill, J. T. Wang, G. Seydoux, U. S. Tulu, D. P. Kiehart, E. Betzig, Lattice light-sheet microscopy: imaging molecules to embryos at high spatiotemporal resolution. *Science*. **346**, 1257998 (2014).

10. S. Liu, M. J. Mlodzianoski, Z. Hu, Y. Ren, K. McElmurry, D. M. Suter, F. Huang, sCMOS noise-correction algorithm for microscopy images. *Nat. Methods*. **14**, 760–761 (2017).

11. T. (2019). Lambert, tlambert03/LLSpy: Lattice light-sheet post-processing utility. *Zenodo* (2019), doi:doi: 10.5281/zenodo.1059099.

12. L. A. Royer, M. Weigert, U. Günther, N. Maghelli, F. Jug, I. F. Sbalzarini, E. W. Myers, ClearVolume: open-source live 3D visualization for light-sheet microscopy. *Nat. Methods*. **12**, 480–481 (2015).

13. A. Dobin, C. A. Davis, F. Schlesinger, J. Drenkow, C. Zaleski, S. Jha, P. Batut, M. Chaisson, T. R. Gingeras, STAR: ultrafast universal RNA-seq aligner. *Bioinformatics*. **29**, 15–21 (2013).

14. Y. C. Lin, S. Jhunjhunwala, C. Benner, S. Heinz, E. Welinder, R. Mansson, M. Sigvardsson, J. Hagman, C. A. Espinoza, J. Dutkowski, T. Ideker, C. K. Glass, C. Murre, A global network of transcription factors, involving E2A, EBF1 and Foxo1, that orchestrates B cell fate. *Nat. Immunol.* **11**, 635–643 (2010).

15. M. B. Eisen, P. T. Spellman, P. O. Brown, D. Botstein, Cluster analysis and display of genome-wide expression patterns. *Proc. Natl. Acad. Sci. U. S. A.* **95**, 14863–14868 (1998).

16. Y. Zhou, B. Zhou, L. Pache, M. Chang, A. H. Khodabakhshi, O. Tanaseichuk, C. Benner,

S. K. Chanda, Metascape provides a biologist-oriented resource for the analysis of systems-level datasets. *Nat. Commun.* **10**, 1523 (2019).

17. W. K. Russell, Z. Y. Park, D. H. Russell, Proteolysis in mixed organic-aqueous solvent systems: applications for peptide mass mapping using mass spectrometry. *Anal. Chem.* **73**, 2682–2685 (2001).

18. D. Giustarini, I. Dalle-Donne, A. Milzani, P. Fanti, R. Rossi, Analysis of GSH and GSSG after derivatization with N-ethylmaleimide. *Nat. Protoc.* **8**, 1660–1669 (2013).

19. D. I. Benjamin, A. Cozzo, X. Ji, L. S. Roberts, S. M. Louie, M. M. Mulvihill, K. Luo, D. K. Nomura, Ether lipid generating enzyme AGPS alters the balance of structural and signaling lipids to fuel cancer pathogenicity. *Proc. Natl. Acad. Sci. U. S. A.* **110**, 14912–14917 (2013).

20. S. M. Louie, E. A. Grossman, L. A. Crawford, L. Ding, R. Camarda, T. R. Huffman, D. K. Miyamoto, A. Goga, E. Weerapana, D. K. Nomura, GSTP1 Is a Driver of Triple-Negative Breast Cancer Cell Metabolism and Pathogenicity. *Cell Chem. Biol.* **23**, 567–578 (2016).

21. K. R. Levental, H. Yu, L. Kass, J. N. Lakins, M. Egeblad, J. T. Erler, S. F. T. Fong, K. Csiszar, A. Giaccia, W. Weninger, M. Yamauchi, D. L. Gasser, V. M. Weaver, Matrix crosslinking forces tumor progression by enhancing integrin signaling. *Cell*. **139**, 891–906 (2009).

A

400 Pa   6k Pa   60k Pa

B 60 kPa (Matrix roGFP2)

Cellular Respirometry
Δ [Fibronectin] Surface Coating

6 μM/cm² Fibronectin Surface Coating
(low ligand density)

C

OCR (pmol/min)

****

6 μM/cm²   60 μM/cm²

D

OCR % Change (Pre/Post Injection)

****

Mg²⁺   Mn²⁺

E

OCR (pmol/min/μg protein)

- Control
- ROCK:ER

****   ****

Basal   Uncoupled   Maximal

F

OCR (pmol/min/ug Protein)

****   ****

Control   ROCK:ER   ROCK:ER + Y27632

G

β1   β1(V737N)

FAK pY397

FAK

H

Vehicle   Mn²⁺   ROCK:ER

β-Actin

HSP90B

MLCpS19

K MDA231

Elastic Modulus (kPa)

***

5 mM   25 mM

I

Relative Expression

- 5 mM
- 25 mM

NRF2 PGC1A ATF5 HSPD1 HSPE1 LONP1 LOX UCP2 HSF1 HSPA9 tFAM hnRNPa1

J

Relative Expression

- 400
- 1k
- 6k
- 60k

NRF2 PGC1A ATF5 HSPD1 HSPE1 LONP1 LOX UCP2 CHOP HSF1 HSPA9 tFAM hnRNPa1
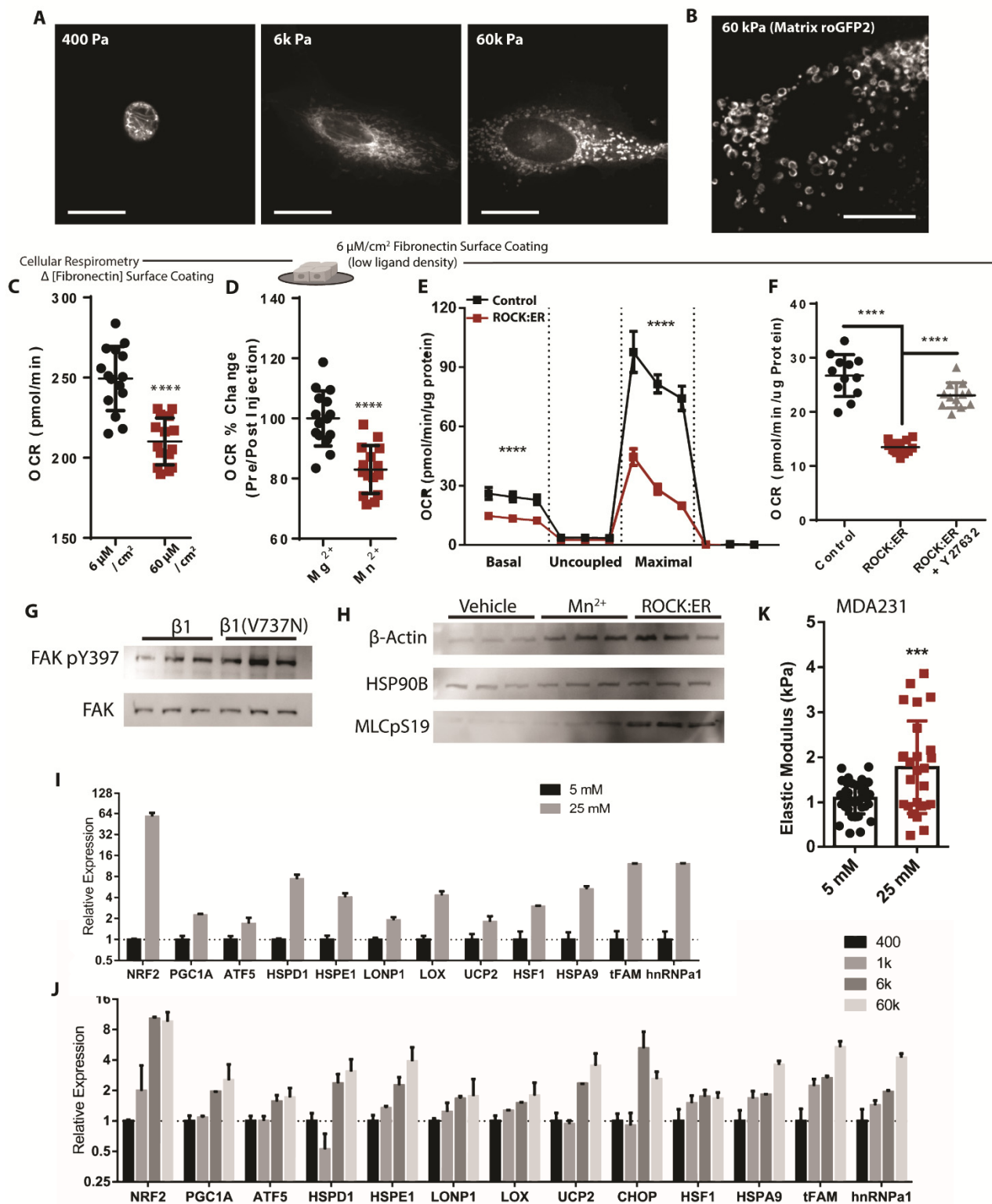
15

Figure S1:

A. Microscopy depicting mitochondrial network structure in single cells cultured on varied elasticity PA-gel surfaces coated with fibronectin [6 µM/cm^2] coating, mitotracker (deep red FM) [100 nM]. (Scale Bar: 10 µm)

B. Representative microscopy depicting mitochondrial network structure in single cells expressing mitochondrial matrix targeted roGFP2 cultured on 60k Pa PA-gel surfaces. (Scale Bar: 10 µm)

C. OCR of cells cultured for 24 h on varied fibronectin surface coating density (n=5 wells, 3 replicate measures).

D. OCR 15 min before and a 15 minutes after the addition of Mn2+ or Mg2+ [1 µM] via injection port (n=5 wells, 3 replicate measures).

E. Mitochondrial stress test of ROCK:ER fusion protein expressing cells activated *via* 4HT [1 µM] treatment for 48 h or vehicle (n=4 wells, 3 replicate measures).

F. OCR of ROCK:ER fusion protein expressing cells activated *via* 4HT [1 µM] treatment for 48 h or vehicle, +/- y27632 [10 µM] (n=4 wells, 3 replicate measures).

G. Western blot depicting relative protein abundance of focal adhesion kinase (FAK) and phosphorylated/active FAK-pY397 within 5 µg of total protein derived from lysates of β1-integrin or β1(V7373N) expressing cells (n=3 separate experiments).

H. Western blot depicting relative protein abundance of β-actin, HSP90B, and ROCK phosphorylated myosin light chain (MLC-pS19) within 5 µg of total protein derived from lysates of ROCK:ER fusion protein expressing cells activated *via* 4HT [1 µM] treatment for 48 h or vehicle +/- 30 min of Mn^2+ [1 µM]. (n=3 separate experiments).

I. Cellular elasticity of MB-MDA-231 cells exposed to 24 h glucose [5 or 25 mM] on fibronectin [6 µM/cm^2] coated glass coverslips, atomic force microscopy (n= 36 indentations across 3 discrete samples).

J. Relative gene expression of MCF10A cells grown of soft PA-gels (400 PA) treated with glucose [5 or 25 mM] media normalized to low glucose media [5 mM], qPCR-ΔΔCT (housekeeping gene: 18s) (n=5 or 4 separate experiments).

K. Relative gene expression of MCF10A cells grown of varied stiffness PA-gels normalized to 400 Pa surface with low glucose media [5 mM], qPCR-ΔΔCT (housekeeping gene: 18s) (n=5 or 4 separate experiments).

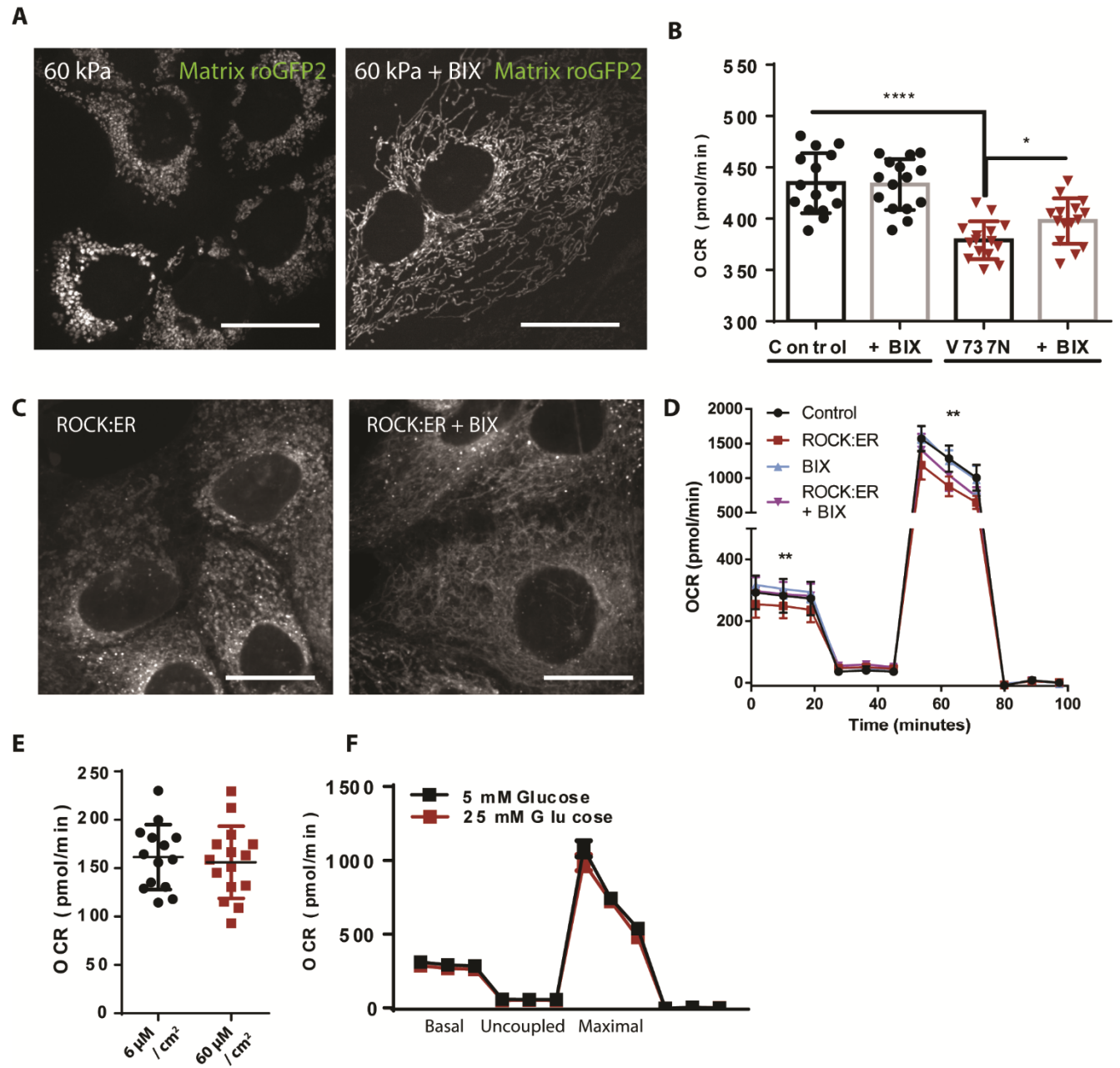Respirometer data shown was repeated at least three separate times with similar results.

A

B

C

D

E

F

Figure S2:

A. Representative microscopy depicting mitochondrial network structure in cells expressing mitochondrial matrix targeted roGFP2 cultured on 60k Pa PA-gel surfaces +/- BIX [500 nM]. (Scale Bar: 10 µm)

B. OCR of β1(V7373N) expressing cells via tetracycline inducible promoter for 24 h with doxycycline [200 ng/mL] +/- BIX [500 nM], (n=5 wells, 3 replicate measures).

E. Representative microscopy depicting mitochondrial network structure in ROCK:ER fusion protein expressing cells activated via 4HT [1 µM] treatment for 48 h or vehicle +/- BIX [500 nM]. (Scale Bar: 10 µm)

D. OCR during a mitochondrial stress test (oligomycin [1 µM], FCCP [1 µM], and antimycin A / rotenone [1 µM]) of ROCK:ER fusion protein expressing cells activated *via* 4HT [1 µM] treatment for 48 h or vehicle, +/- BIX [500 nM] (n=5 wells).

E. Oxygen consumption rate (OCR) of SLC9A1 KO cells in response to glucose [5 or 25 mM] (n=5 wells, 3 replicate measures).

F. Mitochondrial stress test of SLC9A1 KO cells in response to 24 h of varied fibronectin surface coating density (n=5 wells, 3 replicate measures).

Respirometer data shown was repeated at least three separate times with similar results.

18

A Microscopy w/ Mitochondrial Matrix roGFP2
+/- Mitochondrial Calcium Reduction or ROS Quenching
60k — SN-2 — ru360 — MitoTempo

B Mitochondrial ROS Reporter (H_2O_2)
6k PA-gel +/- MitoCalcium Loading

C C. elegans
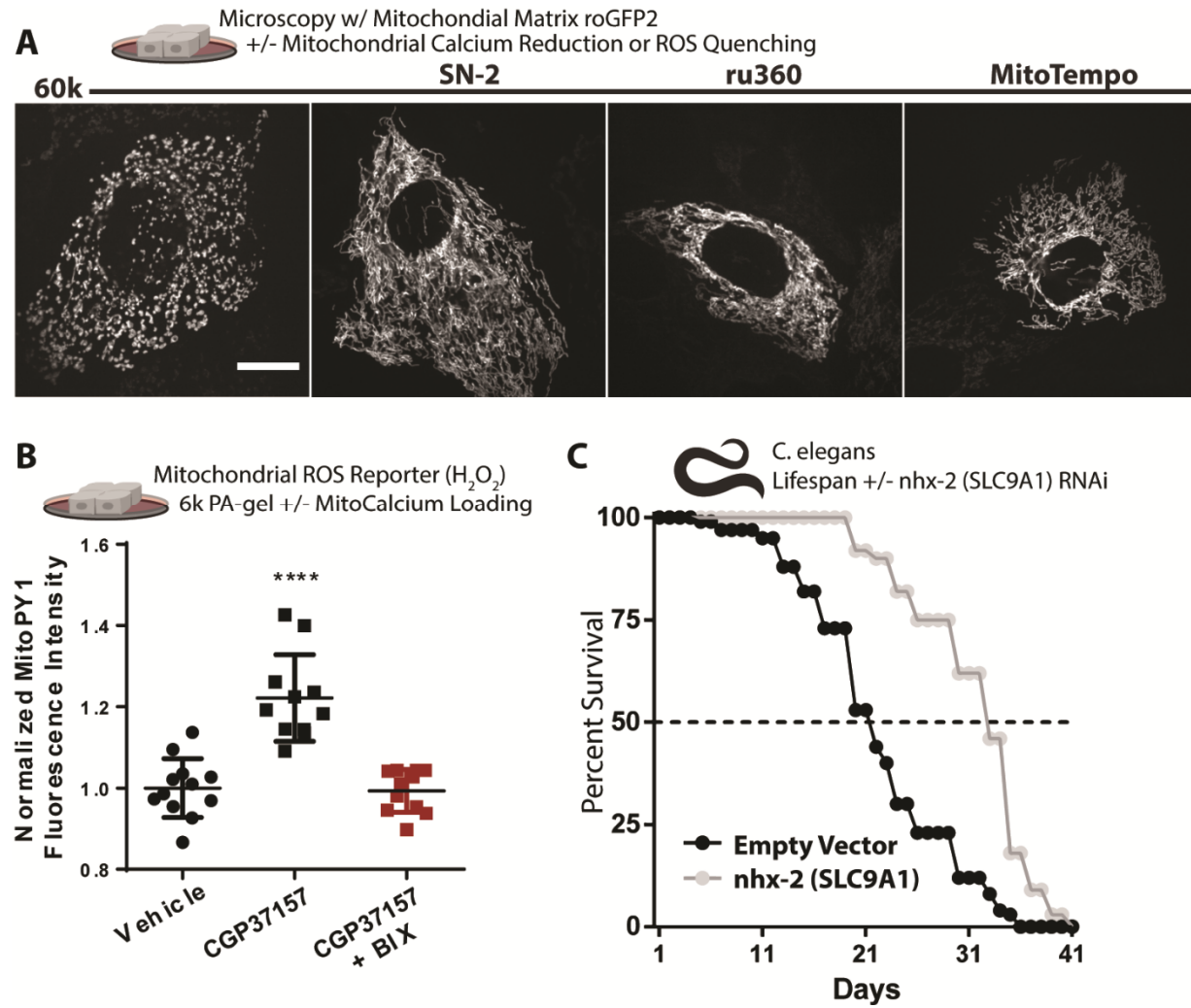Lifespan +/- nhx-2 (SLC9A1) RNAi

Figure S3:

A. Representative microscopy depicting mitochondrial network structure of cells cultured on 60k Pa PA-gel surfaces treated with 1 µM ru360 (MCU inhibitor), 10 µM SN-6 (NCX reverse mode inhibitor, opposite direction of CCP37157), and 2 µM Mitotempo for 24 h. (Scale Bar: 10 µm)

B. Mitochondrial H_2O_2 production of cells cultured on 6k Pa surfaces and treated with BIX [500nM] or vehicle for 24 h and then MitoPy1 [1 µM] and vehicle or CGP37157 [1 µM] for 1 h (n=6, repeated twice).

C. Lifespan of *C. elegans* grown on *nhx-2* (SLC9A1 orthologue) or empty vector RNAi, (n=120 animals, repeated 3 times)
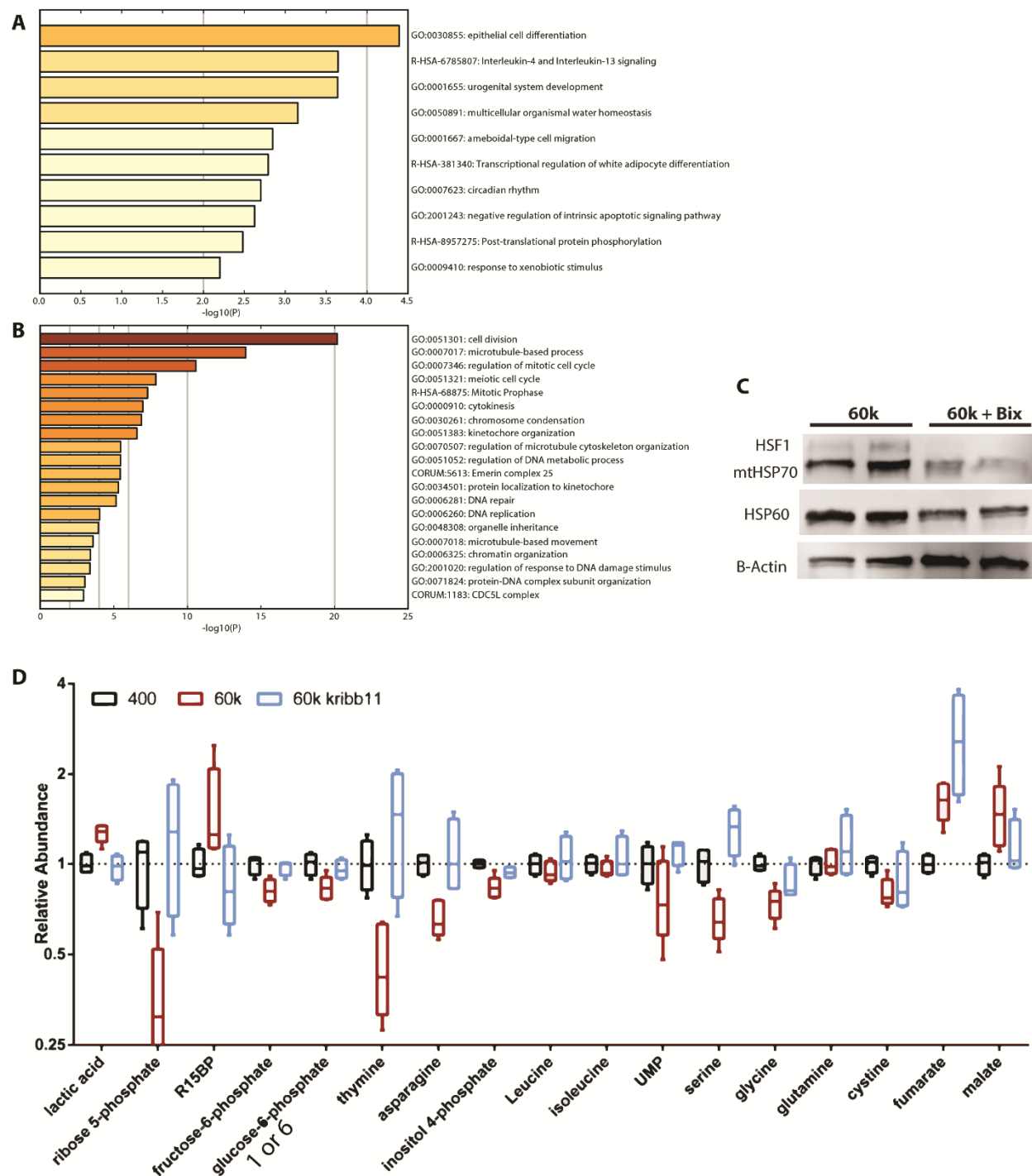
20

A GO:0030855: epithelial cell differentiation
R-HSA-6785807: Interleukin-4 and Interleukin-13 signaling
GO:0001655: urogenital system development
GO:0050891: multicellular organismal water homeostasis
GO:0001667: ameboidal-type cell migration
R-HSA-381340: Transcriptional regulation of white adipocyte differentiation
GO:0007623: circadian rhythm
GO:2001243: negative regulation of intrinsic apoptotic signaling pathway
R-HSA-8957275: Post-translational protein phosphorylation
GO:0009410: response to xenobiotic stimulus

B GO:0051301: cell division
GO:0007017: microtubule-based process
GO:0007346: regulation of mitotic cell cycle
GO:0051321: meiotic cell cycle
R-HSA-68875: Mitotic Prophase
GO:0000910: cytokinesis
GO:0030261: chromosome condensation
GO:0051383: kinetochore organization
GO:0070507: regulation of microtubule cytoskeleton organization
GO:0051052: regulation of DNA metabolic process
CORUM:5613: Emerin complex 25
GO:0034501: protein localization to kinetochore
GO:0006281: DNA repair
GO:0006260: DNA replication
GO:0048308: organelle inheritance
GO:0007018: microtubule-based movement
GO:0006325: chromatin organization
GO:2001020: regulation of response to DNA damage stimulus
GO:0071824: protein-DNA complex subunit organization
CORUM:1183: CDC5L complex

C

D

Figure S4:

A-B. Gene ontology of downregulated genes (top) and upregulated (bottom) from RNAseq of cells cultured on varied elasticity PA-gels for 24 h +/- glucose [5 or 25 mM], (n=2 duplicate libraries of 3 biological replicates, heatmap depicts mean of each condition, ~ 10 million reads per library).

C. Western blot depicting relative protein abundance of 60k Pa PA-gels +/- 500 nM Bix treatment (n=2 two biological replicates shown, repeated three times).

D. Selection of metabolites sensitive to stiffness or KRIBB1111 treatment (n=5 biological replicates), related to Fig. 4D.
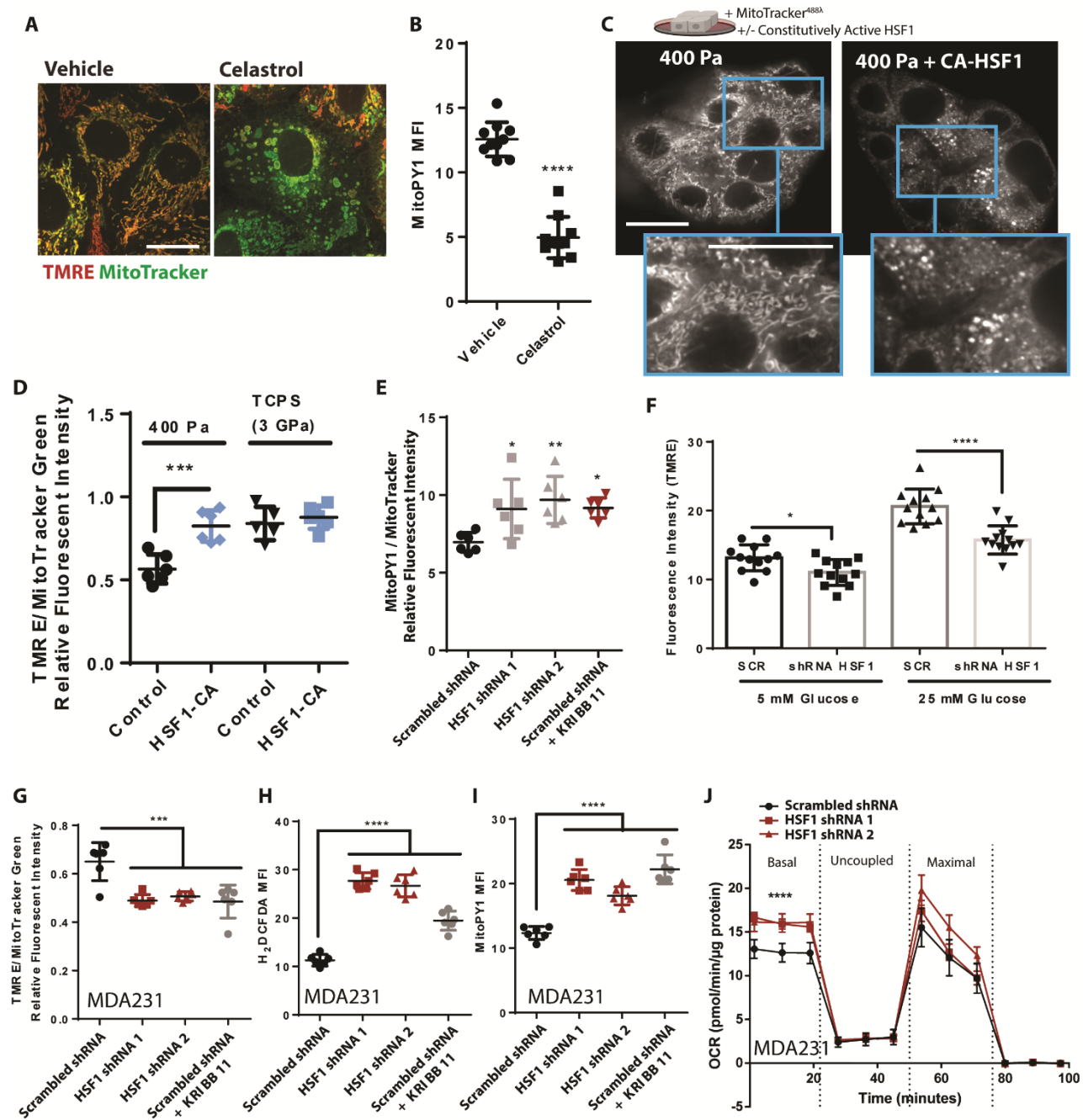
Figure S5:

A. Representative microscopy depicting morphology and mitochondrial membrane potential staining of live cells via TMRE [10 nM] staining and mitotracker (green FM) [100 nM] +/- vehicle or Celastrol [2 μM] treatment for 40 minutes prior to imaging. (Scale Bar: 10 μm)

B. Mitochondrial H_2O_2 production of cells treated with Celastrol [2 μM] treatment for 40 minutes (n=5).

C. Representative microscopy depicting mitochondrial network structure of cells cultured on 400 Pa surfaces expressing constitutively active HSF1 or empty vector control, mitotracker (deep red FM) [100 nM]. (Scale Bar: 10 μm)

D Mitochondrial membrane potential MCF10A cells expressing CA-HSF1 on 400 Pa PA-gels or tissue culture polystyrene (TCPS) surfaces, measured with TMRE [10 nM] after 1 h staining (n=6).

E. Mitochondrial hydrogen peroxide production of MCF10A cells expressing a scrambled shRNA +/- KRIBB11 [2 μM] or two different shRNAs targeting HSF1, measured with MitoPY1 [2 μM] normalized to Mitotracker green staining [100nM].

F. Mitochondrial membrane potential of MDA-231 cells cultured on TCPS expressing a scrambled shRNA +/- shRNAs targeting HSF1 (1) +/- glucose [5 or 25 mM], measured with TMRE [10 nM] after 1 h staining (n=6).

G. Mitochondrial hydrogen peroxide production of MDA-231 cells cells expressing a scrambled shRNA +/- KRIBB11 [2 μM] or two different shRNAs targeting HSF1, measured with MitoPY1 [2 μM] normalized to Mitotracker green staining [100nM].

H. Oxidative stress indicator intensity of of MDA-231 cells expressing a scrambled shRNA +/- KRIBB11 [2 μM] or two different shRNAs targeting HSF1, measured with H_2DCFDA [2 μM]

I. Mitochondrial membrane potential of MDA-231 cells expressing a scrambled shRNA +/- KRIBB11 [2 μM] or shRNAs targeting HSF1 +/- glucose [5 or 25 mM], measured with TMRE [10 nM] after 1 h staining (n=6).

J. Oxygen consumption rate (OCR) of MDA-231 cells expressing a scrambled shRNA or two different shRNAs targeting HSF1 (n=5 wells, 3 replicate measures, repeated three times)

Respirometer data shown was repeated at least three separate times with similar results.
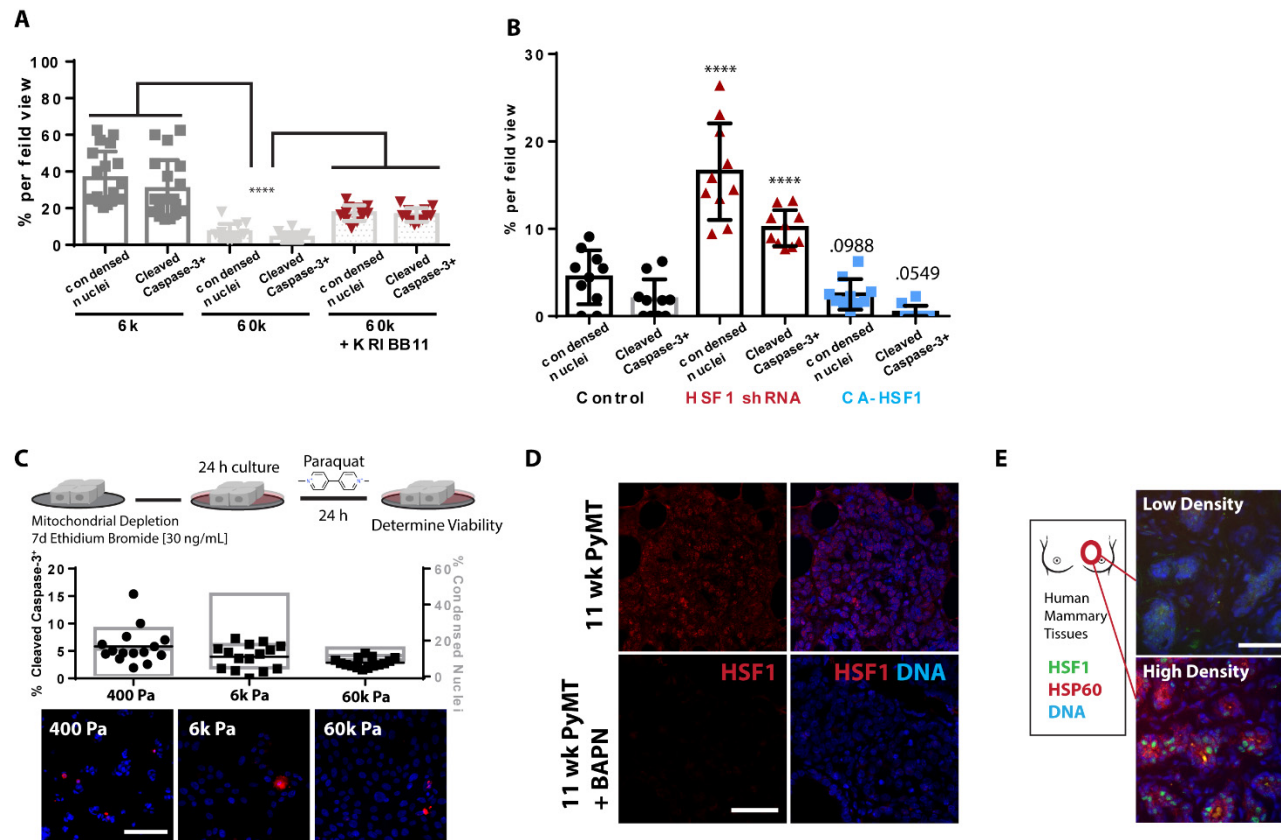
Figure S6

A. Cleaved caspase 3 staining (red) and nuclear condensation (dapi) of cells cultured on 6 or 60 Pa PA-gel surfaces for 24 h +/- vehicle or KRIBB11 [2 µM] followed by 24 h paraquat treatment [10 mM], (n= 16 field views ~ 600 cells per condition, repeated three times)

B. Quantitation of cells from 16 field views depicted in G for condensed nuclei and cleaved caspase-3 positive cells of MCF10A cells cultured on fibronectin coated glass coverslips (~800 cells counted per condition, repeated three times).

C. Representative microscopy and quantitation of indicators of apoptosis with cleaved caspase 3 staining (red) and nuclear condensation (dapi) of MCF10A cells previously cultured for 7 d with 30 ng/mL ethidium bromide in the culture media, then transferred and cultured on 400, 6k, 60k Pa PA-gel surfaces for 24 h with another 24 h +/- paraquat treatment [10 mM]. 100k cells/well of 24 well plate. EtBr maintained in media during paraquat challenge. (~600 cells counted per condition). Repeated three times (Scale Bar: 100 µm)

D. Representative immunofluorescence microscopy of murine mammary tumors derived from mice treated with BAPN, which inhibits Lysyl Oxidase mediated crosslinking of collagen and reduces ECM stiffness (*21*). Immunofluorescence microscopy for HSF1 (red) and DNA (blue). Supporting evidence showing that tumor HSF1 levels and nuclear localization may be sensitive to mechanical stress. (Scale Bar: 100 µm).

E. Representative immunofluorescence microscopy of human mammary glands derived from patient biopsies from low and high density breast tissues stained for HSF1 (green), HSP60 (red), and DNA (blue). In varied density human mammary tissues, HSF1 translocates to the nucleus and enhanced target gene expression in high density tissues supporting the in vitro evidence that HSF1 activity may be sensitive to biophysical signals. (Scale Bar: 100 µm)